NASA Contractor Report 187496
ICASE Report No. 91-1

ICASE

TRANSIENT, HYPERVELOCITY FLOW IN AN AXISYMMETRIC NOZZLE

P. A. Jacobs

Contract No. NAS1-18605
January 1991

Institute for Computer Applications in Science and Engineering
NASA Langley Research Center
Hampton, Virginia 23665-5225

Operated by the Universities Space Research Association

National Aeronautics and
Space Administration

Langley Research Center
Hampton, Virginia 23665-5225

TRANSIENT, HYPERVELOCITY FLOW IN AN AXISYMMETRIC NOZZLE

P. A. Jacobs[1]
Institute for Computer Applications in Science and Engineering
NASA Langley Research Center
Hampton, VA 23665

ABSTRACT

This study examines the performance of an axisymmetric nozzle which was designed to produce uniform, parallel flow with a nominal Mach number of 8. A free-piston-driven shock tube was used to supply the nozzle with high-temperature, high-pressure test gas. Performance was assessed by measuring Pitot pressures across the exit plane of the nozzle and, over the range of operating conditions examined, the nozzle produced satisfactorily test flows. However, there were flow disturbances that persisted for significant times after flow initiation.

The detailed starting process of the nozzle was also investigated by performing numerical simulations at several nominal test conditions. The *classical* description of the starting process, based on a quasi-one-dimensional model, provided a reasonable approximation and was used to demonstrate that the starting process could consume a significant fraction of the otherwise usable test gas. This was especially important at high operating enthalpies where nozzle supply conditions were maintained for shorter times. Multidimensional simulations illustrated a mechanism by which the starting process in the actual nozzle could take longer than that predicted by the quasi-one-dimensional analysis. However, the cause of the persistent disturbances observed in the experimental calibration was not identified.

[1]Research was conducted under NASA Contract No. NAS1-18605 while the author was in residence at the Institute for Computer Applications in Science and Engineering (ICASE), NASA Langley Research Center, Hampton, VA 23665.

1 INTRODUCTION

In recent years there has been a renewal of interest in pulse-type aerodynamic test facilities as a way of providing experimental data for flight Mach numbers above 8. In particular, the free-piston-driven reflected-shock tunnel has emerged as a versatile facility covering the hypervelocity range $10 < M_{flight} < 25$ with sufficient test section density to be useful in combustion studies. See Stalker [1] for a review of pulse facilities and their use in experimental hypervelocity aerodynamics.

When designing experiments for these facilities, the duration of the quasi-steady test flow is often a limiting factor. Typical test times range from $\frac{1}{10}$ to 3 millseconds. From the experimenter's point of view, the model size must be restricted such that the important flow features are allowed to reach steady state in the available test time (see e.g. [2]). From the facility designer's point of view, it is important to make the steady flow duration as long as possible. Therefore, the facility nozzle must not only provide uniform and parallel flow to the test region, it should also start quickly and reach steady state while consuming as little test gas as possible. These constraints become more severe at the higher enthalpies where the facility supplies a smaller amount of test gas for a shorter time.

This paper consists of two major parts. The early sections (2 - 4) consider the design and calibration of an axisymmetric nozzle for the T4 shock tunnel facility [3] located at the University of Queensland, Australia. The nozzle, intended to supply test gas to a model scramjet combustor, was designed using the simple flow decoupling approach described in [4]. The fabricated nozzle was $1.86m$ long, had a $15.24mm$ diameter throat and a $388mm$ diameter exit. Its design Mach number was 8. The nozzle was calibrated by measuring Pitot pressures near the exit plane for a number of operating conditions. In the calibration experiment, it was found that the nozzle flow was taking much longer to reach steady state than initially expected.

The later sections of this paper (5 - 7) describe attempts to numerically simulate the transient starting process of the nozzle. The aim of the simulations was to identify the mechanism which caused the starting delay observed in the experiment. A quasi-one-dimensional method was used to investigate the transient wave structure and the nozzle starting time over a number of tunnel operating conditions while an axisymmetric Navier-Stokes code was used to illustrate the multidimensional and viscous aspects of the starting process.

2 REFLECTED-SHOCK TUNNEL OPERATION

The principal features of a free-piston driven shock tunnel, along with an approximate wave diagram, are shown in Fig. 1. The driver tube, which initially contains low pressure helium downstream of the piston, and the shock tube which contains the test gas, are separated by the primary diaphragm. This diaphragm was typically composed of two sheets of mild steel. Attached to the downstream end of the shock tube is the facility nozzle whose throat is significantly smaller than the inside diameter of the shock tube. The subsonic portion of the nozzle effectively closes the downstream end of the shock tube and forms the shock reflection region. The supersonic portion of the nozzle empties directly into a test section and dump tank which is evacuated to an initial pressure of approximately 30 Pa. The test gas is retained in the shock tube by a thin mylar diaphragm.

The first stage of operation is the launch of the piston and its acceleration along the compression tube. The driving force is supplied by compressed air from a reservoir. The helium in front of the piston is compressed and eventually reaches the same pressure as the compressed air driving the piston. Because of its large kinetic energy, the piston overshoots and further compresses the helium. The primary diaphragm subsequently bursts (at a pressure $56.6MPa$ for a $4mm$ thick diaphragm). At this point, the helium has been compressed to 1/60th of its initial volume and is contained in approximately $0.5m$ of the compression tube. This part of the compression tube then becomes a constant pressure driver section for the shock tube [5].

After rupture of the primary diaphragm, the helium expands into the shock tube and compresses the test gas before it. Unlike the approximately isentropic compression of the helium, the processing of the test gas is performed by a strong normal shock. This *primary* shock wave travels the length of the shock tube, reflects from the closed end, and brings the test gas to rest in the nozzle supply region. Operation in this manner is called *tailored* [6] and is shown in the wave diagram (Fig. 1(b)) by the contact surface coming to rest when intercepted by the reflected shock. The shock-compressed test gas is temporarily contained in the nozzle supply region which has a length of $0.25 - 0.5m$. Ideally the nozzle supply conditions, characterized by the total enthalpy H_s and pressure P_s, are maintained as the reflected shock continues upstream though the driver gas.

Aside from supply pressure fluctuations after shock reflection, the useful test time is terminated by contamination of the test gas by driver gas. The mechanism for this contamination is the bifurcation of the reflected shock into two oblique shocks near the tube wall [7] [8]. While the strong normal shock brings the driver gas to rest in the centre of the tube, the weaker oblique shocks allow gas to jet along the tube walls and prematurely

reach the nozzle supply region. In an effort to delay the arrival of this jet, the shock tube is usually operated in an *undertailored* mode where the reflected shock accelerates into the driver gas and an expansion propagates into the nozzle supply region. This increases the distance between the driver-gas/test-gas interface and the end wall of the shock tube but also results in an unavoidable drop in P_s. The approximate time at which contamination of the test gas is expected to occur at the nozzle throat decreases with increasing stagnation enthalpy (see [1]).

Although the ideal operation of the facility provides constant pressure driver conditions to the shock tube, the effect of finite driver size and non-optimal piston dynamics on the relaxation of P_s is noticeable. These effects result in the long term relaxation of P_s and may also contribute to the early decay of P_s. The net result is a typical nozzle supply pressure history as shown in Fig. 2. The transducer used to obtain this trace was located approximately 8 centimetres upstream of the closed end of the shock tube. Hence, the passage of the primary and reflected shocks are shown as distinct events. Because of the location and limited response time for the transducer, the peak reflection pressure was not recorded. Past the maximum value, P_s continued to decay due to the combined effects of undertailored operation and driver dynamics. For pure helium driver gas and operation considered here, this decay was typically $25 - 30\%$ during a nominal $0.5ms$ test time.

Upon shock reflection, the light secondary diaphragm bursts and some of the test gas following the primary shock expands through the nozzle throat into the divergent part of the nozzle. From the point of view of the nozzle, the shock tube is now a reservoir of stagnant, high-temperature, high-pressure test gas.

The subsequent starting of the nozzle has been examined experimentally and analytically by Amann [9] and Smith [10] [11]. As the primary shock travels down the nozzle it accelerates the very low pressure gas already in the nozzle. However, the primary shock decelerates because of the diverging nozzle walls [12]. Figure 3, based on the quasi-one-dimensional model in [11] illustrates this situation. Test gas which accelerates through the nozzle throat following the primary shock, expands to a very high Mach number and is suddenly decelerated when it encounters the slower primary shock structure. An upstream-facing shock is thus formed and is swept downstream through the nozzle. Between the upstream-facing shock and the steady expansion being established near the throat there is an unsteady expansion, the upstream head of which is being swept downstream with velocity $u - a$. When the unsteady expansion is the last wave to be expelled, the starting time for the nozzle can be approximated from the steady state conditions. For higher initial pressures in the nozzle/test-section, the transit time for the upstream-facing shock will determine the noz-

zle starting time [10] [11]. In the conical and wedge-shaped nozzles studied by Smith, the initial pressure could be significantly higher than the steady-state static pressure without prolonging the starting processes. However, for the Mach 8 contoured nozzle studied here, an initial pressure of a tenth of the steady-state static pressure is sufficient to delay the quasi-one-dimensional starting process.

The quasi-one-dimensional model was considered to be adequate for most practical situations where the divergence angle of the nozzle is small and the design Mach number of the nozzle is not too large. Britan and Vasil'ev [13], [14] have studied two-dimensional situations in which the nozzle divergence angle is large and where multidimensional effects upstream of the throat result in high peak properties at the throat (on a time scale much smaller that the nominal test time). This study will not consider such effects in the subsonic part of the nozzle but will consider the situation where the nozzle is relatively long (when compared to the equivalent conical nozzle with the same initial divergence), has a significantly thick boundary layer, and is operated near conditions where the upstream-facing shock limits the starting time.

3 NOZZLE DESIGN

Once the test gas is brought to rest at the end of the shock tube, it is expanded to the test section conditions in two *conceptually* separate stages. First, the gas is expanded through a conical section to produce a uniform *source* flow and then it is straightened by the contoured section of the nozzle wall such that the flow into the test section is approximately uniform and parallel.

The design point chosen for the Mach 8 nozzle had a nozzle supply pressure $P_s = 30.4MPa$, a supply enthalpy $H_s = 16.2MJ/kg$ and temperature $T_s = 8000K$. The throat diameter $d_* = 15.24mm$ was chosen after some iteration. A conceptual view of the entire nozzle is shown in Fig. 4. For computational convenience, we set the origin of the axial coordinate to the start of the conical expansion (immediately after the throat).

For the subsonic portion of the nozzle, most of the end of the shock-tube had been kept flat and normal to the tube axis so that the shock reflection was well behaved. This was not expected to cause any problem as the area ratio of the nozzle was large ($A_{exit}/A_* \simeq 667$) [15]. The subsonic lead-in to the throat needed to be smooth in order to avoid separation and associated oblique shocks at the beginning of the conical expansion [9]. The throat was a constant diameter section of length d_* and was manufactured from a Beryllium-Copper alloy (B10 or B25). In reference [16] it was indicated that such throats produce good quality

source flow when used in conical nozzles. Also, it was found that these throats resisted erosion better than those with a shorter constant-diameter section or those manufactured from grade 316 stainless steel. In operation, the Be-Cu throats increased in diameter by approximately $0.5mm$ over six shots when the tunnel was operated at $H_s = 10MJ/kg$ and $P_s = 50 - 70MPa$.

The design of the initial conical expansion (region 2, Fig. 4) involved the analysis of the flow as a steady, quasi-one-dimensional chemically reacting flow. Flow properties were determined with the program NENZF [17] in which gas in the nozzle supply region (region 1) upstream of the throat is assumed to be stagnant and in chemical equilibrium. A chemical equilibrium model was also used in the throat but a finite-rate chemistry model was used downstream of the throat. The conical expansion had a cone half-angle of 14° and extended to $x = 0.168m$. At this point, the reactions were assumed frozen and the gas was modelled as a perfect gas with a suitably chosen ratio of specific heats, γ. The flow conditions at the end of the conical expansion were $M_A = u/a = 4.245$ where a is an estimate of the speed of sound. The value $\gamma = 1.38$ was chosen by considering *equivalent* chemically reacting and perfect gas flows through the same quasi-one-dimensional expansion.

The Method-of-Characteristics (MOC) was then used to compute the source flow (region 3), the flow correcting section (region 4) and the uniform flow region (region 5) in a semi-automated way with the program described in [18]. The inlet boundary was specified as uniform source flow at 12 points along the arc AB. The Mach number on the axis at point C was computed to be $M_C = 8.02$ and, beyond this point, was held constant. The solution then stepped downstream along the axis and computed the required flow in region 4 by proceeding upstream along characteristics of the same family as CA. Once the characteristic mesh (Fig. 5) was generated, a streamline was interpolated through the mesh, starting at point A and finishing where it intersected the characteristic CD (which forms the upstream boundary of the uniform test flow region). The data points on the interpolated streamline were then fitted with a cubic-spline function [19] having eight knots and a starting slope specified to match the initial conical expansion. Table 1 displays the coordinates of the knots for the spline function.

The design process described above produces a nozzle with the smallest inviscid design length $L_d = 2.187m$. However, a smoother transition may be obtained by adding a section with a smooth variation of axial Mach number between the end of the source flow region (C) and the start of the uniform test flow region. The length of the fabricated nozzle was later reduced by truncating the design contour at $L_t = 1.8m$ where the characteristic CD intersected the estimated boundary layer edge. Because of the high exit Mach number, L_t

j	x_j (m)	r_j (m)	comment
1	0.16800	0.04951	$dr/dx = 0.2493$
2	0.45648	0.10584	
3	0.74488	0.14208	
4	1.03336	0.16552	
5	1.32176	0.18104	
6	1.61024	0.19040	
7	1.89872	0.19520	
8	2.18712	0.19688	natural end condition

Table 1: Knots for the cubic interpolating spline.

is significantly smaller than L_d.

The final design is shown in cross-section in Fig. 6. Note that the converging (subsonic) region closes off the shock tube to form the shock reflection region. This component of the nozzle is manufactured from high-tensile steel and extends into the diverging section of the nozzle to the axial location $x = 0.18m$. Most of the contoured wall is manufactured from glass-reinforced plastic and is attached to the steel section with an aluminium flange.

4 EXPERIMENTAL CALIBRATION

The performance of the nozzle was evaluated by measuring the Pitot pressure P_{pitot} at planes normal to the nozzle axis and located at $x \simeq 1.8m$ and $x \simeq 2.0m$. Each Pitot probe was fitted with a PCB-112 piezo-electric pressure transducer which measured the stagnation pressure behind a detached shock that formed over the upstream face of the probe. Several probes were mounted in a rake and a number of shots of the shock tunnel were made at each nominal operating condition. Refer to [20] for data recording and analysis details and a complete set of data.

Figure 7 shows the unfiltered histories of both nozzle supply pressure and Pitot pressure on the nozzle axis at $x \simeq 1.8m$. These shots were typical of the ~ 30 shots that were made for this survey. Note that the time origin is arbitrary as the recording device was triggered from the supply pressure signal and had an arbitrary pretrigger delay. All of the traces in Fig. 7 show the impulsive start and subsequent decay as discussed in Section 2. The time delay from shock reflection to the initial rise in the Pitot trace is the time for the primary shock to propagate through the nozzle. The relatively slow initial rise of the Pitot traces is

due to the filling of the probe cavity.

Filtered Pitot pressure traces at a number of radial locations are shown in Fig. 8. Here, the time base has been shifted such that the shock reflection occurred at $t = 0$. The filtering was done taking a *moving average* of the trace over a $0.05ms$ window. Note that, after reaching peak values, the traces near the nozzle axis show a rapid decay down to the levels of the outer traces. Note also the fall-off in average pressure and the decline in quality for the traces at $r > 140mm$. This location appears to be within the boundary layer formed along the nozzle wall.

Although the absolute pressures are changing during the test flow period, a quasi-steady estimate can be obtained by considering Pitot traces normalized by a *time-shifted* supply pressure trace

$$P_{norm} = P_{pitot}(t)/P_s(t - \delta t) \quad , \tag{1}$$

where δt is the nominal transit time of a fluid particle from the shock reflection region to the probe position. Normalized Pitot pressure histories for shots 1405 and 1406 are shown in Fig. 9 where $\delta t = 0.50ms$. The extreme values in the early part of the traces ($t < 0.5ms$) are not significant as the nominal time used in equation 1 is less than the time taken for the starting shock structure to traverse the nozzle.

The traces at $r = 112, 120mm$ illustrate the *classical* starting process in which the shock structure appears first followed by the unsteady expansion fan (the dip at $t = 0.6ms$ and subsequent rise to $t = 1.0ms$) and then steady conditions ($t > 1.2ms$). Toward the nozzle axis the flow establishment is qualitatively different. Starting with the passage of the unsteady expansion ($t \simeq 0.75ms$), there is a large disturbance in the flow which is evident out to a radius $r = 90mm$. Such behaviour was obvious in most (but not all shots) and tended to be less significant at the highest enthalpy condition ($H_s \simeq 16MJ/kg$). For $H_s \geq 10MJ/kg$, the disturbed flow consumed a significant fraction of the available test time.

Figure 10 shows the timing of the events at the exit plane of the nozzle for shots with a nominal supply pressure $P_s \simeq 50MPa$. Predictions for the arrival time of the primary shock (line A) and the time to settle within 10% of steady state (line B) were computed using the quasi-one-dimensional model and the code described in Section 6. The initial pressure within the nozzle was set to $P_{init} = 33Pa$ which is typical of conditions used in the T4 facility. Unfortunately precise values of P_{init} were not recorded. Approximate times for arrival of contaminated gas were taken from [1] and adjusted for the length of this nozzle.

The arrival time of the incident shock was well approximated by the quasi-one-dimensional model except at the $H_s \simeq 6.6MJ/kg$ condition. Here, either transient supply conditions (see

Section 5.2) or higher initial pressures in the test section may account for the differences. The settling time estimates (line B, Fig. 10) were relatively insensitive to either of these influences. In the experimental traces, the passage of the upstream head of the expansion fan was identified as the point (after the shock structure passes) where the normalized Pitot pressure rose to the steady level. (Note that the trace may have exceeded the steady-state value after this time.) These times agree qualitatively with the predictions of the settling times (line B) but were all consistently delayed. As will be seen in Section 7.1, this may be a multidimensional effect associated with the distortion of the upstream-facing shock and the unsteady expansion.

The experimental settling time seemed to occur approximately $0.3ms$ after the passage of the unsteady expansion. At the highest enthalpy ($H_s \simeq 16MJ/kg$) this settling time coincided with the estimated arrival time of the driver gas contamination however, the contamination time estimates were considered conservative and the flow disturbances were relatively small at this condition. Hence, some useful (albeit short) test time was expected to be available.

Once a test time was identified (by starting after the initial flow perturbations and then terminating before the expected time of contamination), a quasi-steady value was computed as the mean value of the filtered and normalized trace over the test period. These mean values, together with standard deviations computed over the same period, are shown in Fig. 11. The profiles are grouped with increasing supply enthalpy to the right and increasing supply pressure to the top. Other than some spurious data points near the nozzle axis, the profiles appear to be satisfactory (for shock tunnel work). If the nozzle contour was not performing well then, disturbances would be expected to focus near the nozzle axis. The stray data points may indicate the existence of such problems.

5 FLOW MODELLING

The goal of the numerical simulations was to provide some insight to the performance of the nozzle in terms of its time to start and its steady-state flow uniformity. The causes of the *late-time* disturbances seen in the Pitot pressure traces were of particular interest.

To achieve this goal, time-dependent simulations were performed with a quasi-one-dimensional (Q1D) code and with an axisymmetric full-Navier-Stokes (FNS) code [21]. The former provided a computationally inexpensive way to explore part of the parameter space for the nozzle operating conditions while the FNS code was used to obtain detailed information on the viscous and multidimensional effects at a single operating condition.

In both approaches the nozzle flow was simplified as follows. The gas in the shock-reflection / nozzle-supply region of the shock tube was assumed to be stagnant and in chemical equilibrium. However, supply conditions were allowed to change with time as governed by the supply pressure trace (Fig. 2). Flow into the nozzle was assumed inviscid, quasi-steady and also in chemical equilibrium. There were no transient or shock-focusing effects [13] considered here. Starting at the throat, the gas was assumed to be a non-reacting mixture of nitrogen and oxygen with mass fractions 0.7686 and 0.2314, respectively. The thermodynamic model [22] was based on weighting the polynomial fits for the individual species. The particular constants and expressions used for the Q1D simulations are given in Appendix A. A further simplification was that only *laminar* flows were considered.

5.1 Geometry

Figure 12 shows flow geometry considered in the simulations. The axis of symmetry is aligned with the x-axis and flow is from left to right, entering through the nozzle throat at $x = 0$ and exiting at the $x = 2.187m$ boundary. The inflow boundary was considered to have uniform, supersonic flow conditions as specified in Section 5.2, while the outflow boundary condition was implemented as a zero-order extrapolation. The $x = 1.8m$ plane was considered far enough upstream of the outflow boundary to be unaffected by the form of the outflow boundary condition, even in the presence of a boundary layer.

The radial position of the wall starts with a value $r_{wall} = 0.00762m$ at $x = 0$, varied linearly with slope $dr/dx = 0.2493$ for $0 < x < 0.168m$ and was defined as a cubic-spline function (see Table 1) for $0.168m < x < 2.187m$. Note that the contoured wall of the fabricated nozzle was truncated at $x = 1.8m$. For the Q1D calculations, the nozzle wall was considered to be an inviscid boundary while, for the FNS calculations, it was considered to be either the same or a no-slip constant-temperature ($T_{wall} = 300K$) boundary. A constant-temperature boundary was considered appropriate because the surface temperature of the wall was expected to rise no more than a few degrees (say, $< 10K$) above room temperature for the duration of the test flow [23].

5.2 Inflow and Initial Conditions

The inflow condition at $x = 0$ was set to approximate the throat conditions in the T4 facility at the nominal operating condition with a $4mm$ mild steel primary diaphragm, a driver tube compression ratio $\lambda = 60$, and the shock tube initially filled with air at $P = 120kPa$ and $T = 296K$. The flow conditions at the beginning of the conical expansion were obtained with the following procedure.

Step 1: The supply conditions (behind the reflected shock) were estimated with the program ESTC [24] which incorporated an equilibrium chemistry model for air with the species N_2, N, O_2, O, NO, NO^+ and e^-. From the shock reflection conditions, the test gas was allowed to expand adiabatically in chemical equilibrium to the measured *equilibrium* supply pressure [15]. From Fig. 13, the equilibrium pressure was estimated to be $P_{s-ref} \simeq 50MPa$ at $t = 3.4ms$ thus giving an equilibrium stagnation enthalpy $H_{s-ref} \simeq 10MJ/kg$ and temperature $T_{s-ref} \simeq 6010K$.

Step 2: Using these reference conditions, flow at the throat was estimated using the quasi-one-dimensional code NENZF [17] in which the test gas was again assumed to be in equilibrium. Conditions at the throat consistent with the $N_2 - O_2$ mixture were: temperature $T_* = 5448K$, pressure $P_* = 27.94MPa$, density $\rho_* = 17.79kg/m^3$, velocity $u_* = 1450m/s$, and specific internal energy $e_* = 5.24MJ/kg$.

Step 3: A *transient* inflow was constructed from the supply pressure history by using ESTC and NENZF to compute the quasi-steady throat conditions for a number of P_s values. The control points, labelled a through d in Table 2, divided the supply pressure trace into three convenient segments, the first two of which were specified as the cubic

$$P_s = \alpha_3\tau^3 + \alpha_2\tau^2 + \alpha_1\tau + \alpha_0, \tag{2}$$

where the α_i and τ are defined in Table 3 and $t < t_c$. When $t > t_c$, the supply pressure followed the exponential decay

$$P_s = P_c exp(-\alpha_4(t - t_c)), \tag{3}$$

where

$$\alpha_4 = \frac{-log_e(P_d/P_c)}{(t_d - t_c)}. \tag{4}$$

Figure 13 shows a comparison between these approximate expressions for supply pressure and the measured (filtered) supply pressure trace for shot 1405. The quasi-steady supply temperature was found to be well approximated by the perfect gas relation

$$\left(\frac{T_s}{T_{s-ref}}\right) = \left(\frac{P_s}{P_{s-ref}}\right)^{(\gamma-1)/\gamma} \tag{5}$$

where the effective ratio of specific heats is $\gamma = 1.197$ and the reference conditions are the nominal supply conditions given above.

Step 4: The conditions at the nozzle throat were then related to the transient value of P_s with the following correlations

$$P_*/P_s = 0.559,$$

Label	t (ms)	P (MPa)
a	0.0	11.4
b	0.152	57.3
c	0.464	48.0
d	1.149	26.7

Table 2: Control points for the transient P_s expressions.

Parameter	$t_a < t < t_b$	$t_b < t < t_c$
τ	$(t - t_a)/(t_b - t_a)$	$(t - t_b)/(t_c - t_b)$
α_0	P_a	P_b
α_1	$\frac{3}{2}(P_b - P_a)$	0
α_2	0	$\frac{3}{2}(P_c - P_b)$
α_3	$\frac{1}{2}(P_a - P_b)$	$\frac{1}{2}(P_b - P_c)$

Table 3: Parameters for the transient supply pressure equation.

$$
\begin{aligned}
T_*/T_s &= 0.907, \\
\rho_*/\rho_s &= 0.624, \\
u_*/a_s &= 1.050,
\end{aligned}
\tag{6}
$$

where $a_s = (317.0 * T_s)^{1/2}$. Other properties are obtained from the thermodynamic model for the $N_2 - O_2$ mixture. Figure 14 shows the variation of these properties with time. Note that, while the throat pressure and density drop approximately 30% from $t = 0.5ms$ to $t = 1.0ms$, the temperature and velocity drop by only 7.5% and 5%, respectively.

Initial conditions in the nozzle (and facility test section) were set to $T_{init} = 300K$, $u_{init} = 0$ and $33Pa < P_{init} < 150Pa$. The lower values of $P_{init} = 33Pa$ were typical of the facility operating conditions but the higher pressures may occur in the presence of test section leaks or when hydrogen-fueled scramjet models are being tested. For such tests, hydrogen fuel is injected into the model (and test section) several milliseconds before the flow through the nozzle is started.

6 QUASI-ONE-DIMENSIONAL SIMULATIONS

The quasi-one-dimensional simulations were performed for a single nozzle supply condition $H_{s-ref} = 10MJ/kg$ with $P_{s-ref} = 50MPa$. Initial pressures ranged from $P_{init} = 33Pa$ to $P_{init} = 300Pa$. The lower values of P_{init} are representative of actual facility operating conditions while the higher values were performed for comparison with the axisymmetric simulations.

The code used a simple finite-volume formulation which was second order accurate in both space and time. An Osher-type Riemann solver [25] was used to obtain interface fluxes and a SUPERBEE limiter [26] was used to interpolate flow properties. The implementation is more fully described in Appendix B.

In all of the simulations reported here, the computational cells were arranged with equal increments in x, and time stepping was done with a CFL number of approximately 0.25. Simulations with 250 cells were used to obtain the timing data shown in Fig. 10 while simulations with 500 cells were used to obtain the results discussed below. There was little difference (i.e. $< 1\%$) between both sets of solutions in terms of both wave speeds and steady-state conditions.

6.1 Results

Figure 15 shows time sequences of (logarithmic) density profiles for $P_{init} = 33Pa$ and $150Pa$. Steady inflow conditions were maintained at the throat. All of the major features of Smith's [11] quasi-one-dimensional model appeared. For $P_{init} = 33Pa$, the unsteady expansion was the last wave to sweep through the nozzle but, for $P_{init} = 150Pa$, the unsteady expansion has merged into the upstream-facing shock before this shock reaches $x = 1.8m$. Hence, the $33Pa$ simulation provided an example of the minimum starting time while the slower waves in the $150Pa$ simulation prolonged the starting process. Note that $P_{init} = 150Pa$ was well below the steady-state static pressure of $1667Pa$ that eventually developed at the nozzle exit.

This was a quite different behaviour to that of the conical and wedge nozzles studied in [11] where P_{init} could be significantly larger than the steady-state static pressure without prolonging the starting process. The key difference in the flow geometry is the (necessarily) long contoured section of the nozzle which allows the unsteady expansion to catch (and merge into) the slower moving shock structure. This is shown clearly in Fig. 16 where the wave trajectories (obtained from Fig. 15) are plotted for a number of initial pressures. The trajectory of the upstream head of the unsteady expansion is essentially the same in all cases but the starting shock structure slows significantly for higher values of P_{init}.

Simulations were also performed with transient throat conditions as described in Section 5.2. A summary of times, for arrival of the primary shock at $x = 1.8m$ and the passage of the upstream head of the unsteady expansion at the same point is shown in Fig. 17. Transition from a minimum starting-time condition (limited by the unsteady expansion) to a condition limited by the upstream-facing shock occurs in the range $60Pa < P_{init} < 120Pa$. The ranges of event times for the experimental data are shown as the hatched regions. The primary shock arrival time is well approximated by the steady inflow simulations (in preference to the transient inflow conditions). This may be caused by the omission of the very high peak pressures from the transient inflow specification and the shock focusing effects examined by Britan and Vasil'ev [13]. Both of these effects would result in faster primary shocks. The arrival of the upsteam head of the unsteady expansion occurred at a later time than that predicted by either of the inflow conditions. This delay may be attributed to multidimensional effects as discussed in Section 7.1.

Histories of the simulated Pitot pressure for both steady and unsteady throat conditions are compared with a typical experimental measurement in Fig. 18. The time base for the experimental data has been shifted to put the shock reflection (in the nozzle supply region) at approximately $t = 0$. The Pitot pressure displayed for the simulations was computed with

the approximate relation

$$P_{pitot} = 0.92\rho u^2 \ , \tag{7}$$

which is suitable for high Mach number flow. For the moment, ignore the differences in steady state levels as these may be attributed to boundary layer effects not included in the quasi-one-dimensional simulations. The arival times of primary shock, upstream-facing shock and expansion fan are reasonably close. However, the disturbance in the experimental data from $t = 0.7ms$ to $1.0ms$ has no counterpart in the quasi-one-dimensional numerical simulations.

7 AXISYMMETRIC SIMULATIONS

The axisymmetric simulations were performed in the hope of identifying multidimensional or viscous mechanisms causing the persistent disturbances seen in the Pitot pressure histories of the experimental calibration (cf. Fig. 18b). Two simulations were performed with $P_{init} = 150Pa$ and the steady throat conditions described in Section 5.2. One used an inviscid wall boundary condition while the second used a no-slip, constant temperature boundary condition.

The simulations were performed with an axisymmetric version of the SPARK code [21] which is a finite-difference program that integrates the conservation equations for mass, momentum, energy and species in a time-accurate manner. Along the x-axis, the singular governing equations were collapsed using L'Hopital's rule. The option selected for the time integration was the second-order MacCormack scheme with a CFL number of 0.6. Numerical damping was implemented as a mixture of a standard 4th order artificial dissipation (25%) and a *total-variation-diminishing* dissipation term (75%) [27] based on static pressure only. The dissipation coefficient needed to be set to a value of 1.0 to stabilize the calculation in the presence of the very strong primary shock which, at early times, had a Mach number of ~ 15.

The computational grids were assembled from two zones in which the axial and radial node distributions were generated independently using one of Roberts' [28] stretching transformations. (See also [29], Section 5-b.1). In each zone there were $N + 1$ nodes, including the end points, located at

$$z = z_a\bar{\eta} + z_b(1 - \bar{\eta}) \ , \tag{8}$$

where

$$\bar{\eta} = \frac{[(\beta + 2\alpha)\lambda - \beta + 2\alpha]}{(2\alpha + 1)[1 + \lambda]} \ ,$$

(a)

Axial Zone	α	β	N
$0 < x < 0.2m$	0	1.04	100
$0.2 < x < 2.187m$	0	10.0	494

(b)

Wall Condition	α	β	N
Inviscid	0.5	100	50
Viscous	0.5	1.1	80

Table 4: Grid generation parameters. (a) Axial distribution. (b) Radial distribution.

$$\lambda = \left(\frac{\beta+1}{\beta-1}\right)^{(\eta-\alpha)/(1-\alpha)} , \tag{9}$$

$$\eta = \frac{j}{N},\ j = 0...N\ .$$

Details of the zonal boundaries and stretching parameters are given in Table 4. The same axial distribution was used for both inviscid-wall and viscous-wall solutions. The axial resolution of the grids was determined by the need to ensure conservation in the initial conical expansion and then to retain adequate resolution of the starting shock structure as the structure was swept through the nozzle. The radial grid distribution for the viscous-wall solution was quite different from that of the inviscid solution. While a uniform distribution of $N = 50$ points was found to be adequate for the inviscid solution, the viscous grid had $N = 80$ and was stretched to cluster nodes close to the wall to resolve the boundary layer. However, the number of nodes used and the clustering specified was something of a compromise and the calculation did not adequately resolve the boundary layer in the early part of the expansion.

It should also be noted that (1) zero-gradient boundary conditions were implemented as zero-order extrapolations and (2) zero-gradient boundary conditions at the wall were implemented by specifying the derivatives with respect to the y-coordinate (rather than normal to the wall). Future calculations will be performed on a modified grid with grid lines normal to the wall.

7.1 Results

Figures 19 and 20 show sequences of Mach number contours for the inviscid-wall and viscous-wall simulations, respectively. The initial pressure $P_{init} = 150Pa$ is higher than typically used in the facility, but was the smallest value that could be used with moderate levels of artificial diffusion. As a result, the unsteady expansion was only evident in the solutions up to $t = 0.3ms$. See, for example, the "turning up" of the Mach contours at $t = 0.3ms$ and $x = 0.9m$ in Fig. 19. Beyond that time, the upstream-facing shock became the limiting wave for steady flow.

The most obvious multidimensional effect shown in the inviscid-wall solution is the distortion of the contact discontinuity and the upstream-facing shock into waves that are not planar. The distortion is enough to delay the flow settling time by approximately $0.04ms$ beyond that computed in the Q1D results. This is approximately the size of the delay between the Q1D results and the experimental values as shown in Fig. 17. Although the contact discontinuity was distorted severely, the primary shock remained nearly planar and its speed matched that computed in the Q1D results (cf. Fig. 15).

The introduction of viscous effects caused a thick boundary layer to develop along the nozzle wall (see Fig. 20). The starting shock structure remained essentially the same, with the primary shock again nearly planar. At $t = 0.511ms$ the primary shock arrived at $x = 1.8m$ and had a speed of $3214m/s$. The upstream-facing shock arrived later at $t = 0.643ms$ with a speed of $2643m/s$. The low pressure gas which passed through the primary shock and accumulated before the contact discontinuity, had a Mach number of approximately 2. This is fairly close to the one-dimensional Mach number limit for an infinitely strong shock compression (see e.g. [30])

$$M = \left(\frac{2}{\gamma(\gamma-1)}\right)^{1/2} \simeq 1.89,$$

with $\gamma = 1.4$.

Further details of the starting shock structure are shown in figures 21 and 22. The static pressure contours identify the primary shock and the upstream-facing shock. Alternatively, the temperature field identifies the contact discontinuity and the boundary layer with its large temperature gradients. The static pressure is essentially constant across both of these features. The density field, being sensitive to both pressure and temperature, is more complicated and shows all of the flow features. The velocity field shows abrupt changes at the two shocks and complex recirculation regions between them. It also shows the formation of the boundary layer (for $x < 1.75$ at $t = 0.6ms$) by the entrainment of gas along the wall [31] [23].

Figure 23 shows the evolution of the total boundary-layer thickness δ (as measured by the 99% point in the total enthalpy $H = h + 0.5u^2$ profile), the displacement thickness δ^* and the momentum thickness θ as defined by the expressions [32]

$$r_{wall}^2 - (r_{wall} - \delta^*)^2 = 2\int_{r_{wall}-\delta}^{r_{wall}} \left(1 - \frac{\rho u}{\rho_e u_e}\right) r \, dr \,, \tag{10}$$

$$r_{wall}^2 - (r_{wall} - \theta)^2 = 2\int_{r_{wall}-\delta}^{r_{wall}} \frac{\rho u}{\rho_e u_e}\left(1 - \frac{u}{u_e}\right) r \, dr \,. \tag{11}$$

The total thickness and the displacement thickness settle to a steady state shortly after the passage of the upstream-facing shock. The momentum thickness, however, takes a significantly longer time to settle. At $t = 0.6ms$, the upstream-facing shock has reached $x \simeq 1.7m$ while only the first $0.6m$ of the momentum thickness profile has reached steady state. This agrees reasonably well with the settling time correlations reported in [33].

By $t = 1.2ms$ the boundary layer has approached steady state and δ appears to be a linear function of x, reaching $\delta \simeq 46mm$ at $x = 1.8m$. The displacement thickness remains small for $x < 1.0m$ but then grows linearly (in x) to reach approximately 0.5δ at the nozzle exit. The small initial growth rate for $x < 0.8m$ is due to the combination of the hot free-stream conditions and the relatively cold wall ($300°K$). Momentum thickness grows most rapidly while the displacement thickness is small but levels off once δ^* begins to grow rapidly. At $x = 1.8m$ the displacement thickness and momentum thickness are approximately $23mm$ and $3.2mm$, respectively.

The Pitot pressure, as computed by Eqn.(7), is shown in Fig. 24. Although the traces are somewhat noisy, the starting shock structure is obvious. The settling of the traces ($r = 112$) from the passage of the upstream-facing shock to $t = 0.8ms$ is probably caused by the settling of the boundary layer along the nozzle wall. Unfortunately, the large and persistent disturbances seen in the experimental data are not seen even in these two-dimensional simulations. Unsteady inflow conditions and fully three-dimensional flow models have yet to be investigated.

The radial distributions of Pitot pressure are compared with quasi-steady experimental values in Fig. 25. At $x = 1.8m$ the computed values for the viscous wall simulation fortuitously capture the spurious data points at the nozzle axis. Although the bulk of the computed values are reliable and match the experimental values well, those near the nozzle axis are subject to a particularly noisy boundary condition and should not be trusted. At $x = 2.0m$ there is obvious disagreement with the experiment near the axis. The experimental results also indicate that the physical boundary layer is thicker than that computed in the viscous-wall simulation. Note that the simulation was for laminar flow only whereas the physical flow may have been partly turbulent.

8 CONCLUDING REMARKS

From the experimental point of view, the nozzle appears to produce a satisfactory test flow once it has settled to a (quasi-)steady state. Hence, the simple inviscid design approach is adequate but would benefit from the addition of a boundary layer correction. It may be

possible to partially compensate for this oversight by manufacturing throats with smaller diameters while maintaining the current dimensions of the contoured expansion.

Although the steady performance is adequate, the settling times are much longer than predicted by the *classical* quasi-one-dimensional models. This delay in flow establishment is especially important at high enthalpy ($H_s > 16MJ/kg$) operating conditions as the nozzle supply conditions are maintained for relatively short times after shock reflection. Fortunately, this problem is compensated by the magnitude of the disturbances becoming small at higher H_s.

From the computational point of view, the nozzle starting processes are not fully understood. The quasi-one-dimensional model appears to provide an adequate description of the starting shock structure but fails to predict the long settling times observed in the experiment. The axisymmetric simulations show that, while the primary shock remain nearly planar, the contact discontinuity and the upstream-facing shock are distorted. This distortion is responsible for slightly delaying their arrival at the nozzle exit plane (beyond the times indicated by the quasi-one-dimensional model). However, the axisymmetric simulations did not provide any further insight to the mechanism behind the persistent disturbances seen in the experimental data. Further simulations need to be performed which may include (a) the dynamics of the nozzle supply region (i.e. the shock reflection region of the shock tube); and/or (b) fully three-dimensional effects (starting with a slightly elliptic throat).

Acknowledgments

The design, fabrication and calibration of the nozzle were done at the University of Queensland under the supervision of Prof. Ray Stalker and Richard Morgan. Peter Killen and Ken Dudson fabricated the nozzle. Financial support was provided by the Australian Research Council and NASA[2].

The numerical simulations were done at ICASE, NASA Langley Research Center[3]. Mark Carpenter (Theoretical Flow Physics Branch) provided the axisymmetric version of the SPARK Navier Stokes code and advice on its application. John Korte, Jeff White (TFPB) and Jeff Scroggs (ICASE) provided welcome advice.

[2]grant NAGW-674
[3]contract NAS1-18605

Notation

a : speed of sound
A : interface area (Q1D code)
c : thermodynamic polynomial coefficients (Appendix A)
d : diameter
e : specific internal energy
E : total energy
f : density weighting parameter (Q1D code)
H : total enthalpy
L : nozzle length
M : Mach number
N : number of computational nodes/cells
P : pressure
r : radial coordinate
T : temperature
t : time
u : axial velocity
$\overline{U}$: Riemann invariant (Q1D code)
v : radial velocity
V : cell volume (Q1D code)
w : wave velocity (Q1D code)
x : axial coordinate
X, Y : thermodynamic properties (Appendix A)
Z : intermediate quantity (Q1D code)

α : transient inflow parameter
α, β : coordinate stretching parameters
γ : ratio of specific heats
δt : time delay for normalizing
δ : boundary layer thickness
δ^* : boundary layer displacement thickness
λ : intermediate coordinate; driver tube compression ratio
ρ : density
τ : normalized time (transient inflow parameter)
η : radial computational coordinate
ξ : axial computational coordinate

Subscripts:

$*$	: throat condition
a, b, c, d	: labels (transient inflow description)
A, B, C, D	: locations in the inviscid design
d	: inviscid design value
e	: free-stream conditions
L, R	: left and right states (Q1D code)
s	: nozzle supply/stagnation condition
$s - ref$	: reference supply/stagnation condition
t	: truncated nozzle value
$wall$	: value at the nozzle wall

Superscripts:

$*$: intermediate states (Q1D code)

References

[1] R. J. Stalker. Hypervelocity aerodynamics with chemical nonequilibrium. *Annual Review of Fluid Mechanics*, 21:37–60, 1989.

[2] P. A. Jacobs, R. C. Rogers, E. H. Weidner, and R. D. Bittner. Flow establishment in a generic scramjet combustor. AIAA Paper 90-2096, 1990.

[3] R. J. Stalker and R. G. Morgan. The University of Queensland free piston shock tunnel T4 - initial operation and preliminary calibration. unpublished, Department of Mechanical Engineering, University of Queensland., 1988.

[4] P. A. Jacobs and R. J. Stalker. Design of axisymmetric nozzles for reflected shock tunnels. Department of Mechanical Engineering Report 1/89, University of Queensland, 1989.

[5] R. J. Stalker. A study of the free-piston shock tunnel. *A.I.A.A. Journal*, 5(12):2160–2165, 1967.

[6] C. E. Wittliff, M. R. Wilson, and A. Hertzberg. The tailored-interface hypersonic shock tunnel. *J. Aerospace Sci.*, 26:219–228, 1959.

[7] L. Davies and J. L. Wilson. Influence of reflected shock and boundary-layer interaction on shock-tube flows. *The Physics of Fluids Supplement 1*, pages I–37 – I–43, 1969.

[8] R. J. Stalker and K. C. A. Crane. Driver gas contamination in a high enthalpy reflected shock tunnel. *A.I.A.A. Journal*, 16(3):277–279, 1978.

[9] H. O. Amann. Experimental study of the starting process in a reflection nozzle. *The Physics of Fluids Supplement I*, pages I–150 – I–153, 1969.

[10] C. E. Smith. An analytical study of the starting process in a hypersonic nozzle. In *Proceedings of the 1964 Heat transfer and Fluid Mechanics Institute*, pages 198–210, 1964.

[11] C. E. Smith. The starting process in a hypersonic nozzle. *Journal of Fluid Mechanics*, 24:625–640, 1966.

[12] R. F. Chisnell. The motion of a shock wave in a channel, with applications to cylindrical and spherical shock waves. *Journal of Fluid Mechanics*, 2:286–298, 1957.

[13] A. B. Britan and E. I. Vasil'ev. Pecularities of the formation of the flow in a shaped shock-tube nozzle. *Soviet Physics Doklady*, 30(3):199–201, 1985.

[14] A. B. Britan and E. I. Vasil'ev. Investigation of the starting process in the shaped nozzle of a large-diameter shock tube. *Izvestiya Academii Nauk SSSR*, 5:88–95, 1986.

[15] J. Lukasiewicz. *Experimental Methods of Hypersonics*. Marcel Dekker, New York, 1973.

[16] D. Zonars. Nonequilibrium regime of airflows in contoured nozzles: theory and experiment. *A.I.A.A. Journal*, 4(1):57–63, 1967.

[17] J. A. Lordi, R. E. Mates, and J. R. Moselle. Computer program for the numerical solution of nonequilibrium expansions of reacting gas mixtures. NASA Contractor Report 472, 1966.

[18] P. A. Jacobs. An interactive graphics program for computer assisted calculations of isentropic flows. Department of Mechanical Engineering Report 7/88, University of Queensland, 1988.

[19] G. E. Forsythe, M. A. Malcolm, and C. B. Moler. *Computer methods for Mathematical Computations*. Prentice-Hall, Englewood Cliffs, N. J., 1977.

[20] P. A. Jacobs. A Mach 8 nozzle for the T4 shock tunnel. Department of Mechanical Engineering Report 12/89, University of Queensland, 1989.

[21] J. P. Drummond. A two-dimensional numerical simulation of a supersonic, chemically reacting mixing layer. NASA Technical Memorandum 4055, 1988.

[22] M. H. Carpenter. A generalized chemistry version of SPARK. NASA Contractor Report 4196, 1988.

[23] H. Mirels. Turbulent boundary layer behind constant velocity shock including wall blowing effects. *A.I.A.A. Journal*, 22(8):1042–1047, 1984.

[24] M. K. McIntosh. Computer program for the numerical calculation of frozen and equilibrium conditions in shock tunnels. Technical report, Australian National University, 1968.

[25] S. Osher and F. Solomon. Upwind difference schemes for hyperbolic systems of conservation laws. *Mathematics of Computation*, 38(158):339–374, 1982.

[26] P. L. Roe. Some contributions to the modelling of discontinuous flows. In *Lectures in Applied Mathematics, Volume 22.*, pages 163–193, 1985.

[27] R. C. Swanson and E. Turkel. On central-difference and upwind schemes. ICASE Report 90-44, 1990.

[28] G. O. Roberts. Computational meshes for boundary layer problems. In *Lecture Notes in Physics, 8*, pages 171–177. Springer-Verlag, 1971.

[29] D. A. Anderson, J. C. Tannehill, and R. H. Pletcher. *Computational Fluid Mechanics and Heat Transfer.* Hemisphere, New York, 1984.

[30] J. D. Anderson. *Modern Compressible Flow: with Historical Perspective.* McGraw-Hill, New York, 1982.

[31] H. Mirels. Shock tube test time limitation due to turbulent-wall boundary layer. *A.I.A.A. Journal*, 2(1):84–93, 1964.

[32] F. M. White. *Viscous Fluid Flow.* McGraw-Hill, New York, 1974.

[33] W. R. Davies and L. Bernstein. Heat transfer and transition to turbulence in the shock-induced boundary layer on a semi-infinite flat plate. *Journal of Fluid Mechanics*, 36(1):87–112, 1969.

[34] J. J. Gottlieb and C. P. T. Groth. Assessment of Riemann solvers for unsteady one-dimensional inviscid flows of perfect gas. *Journal of Computational Physics*, 78(2):437–458, 1988.

[35] T. A. Edwards. The effect of exhaust plume/ afterbody interaction on installed scramjet performance. NASA Technical Memorandum 101033, 1988.

(a)

Y	Units	X	Units	X_{min}	X_{max}	Extrapolation
h/e	-	e	MJ/kg	0.5223	4.7609	constant
T	$K/1000$	e	MJ/kg	0.5223	4.7609	linear
e	MJ/kg	T	$K/1000$	0.7215	5.0	linear

(b)

Y	X	c_0	c_1	c_2
h/e	e	0.441746	-1.014804×10^{-1}	3.458821×10^{-2}
T	e	3.370113×10^{-2}	1.426067	-0.236355
e	T	4.937905×10^{-3}	0.614562	0.164100

(c)

Y	X	c_3	c_4	c_5
h/e	e	-6.077331×10^{-3}	4.211913×10^{-4}	0
T	e	6.481913×10^{-2}	-9.236112×10^{-3}	5.254391×10^{-4}
e	T	-3.273006×10^{-2}	3.273170×10^{-3}	-1.196175×10^{-4}

Table 5: Fitted ranges and coefficients for the thermodynamic properties.

A Thermodynamic Model

The thermodynamic model used in the quasi-one-dimensional code assumed a non-reacting mixture of nitrogen and oxygen with mass fractions 0.7686 and 0.2314, respectively. The specific heats for each component were assumed to be functions of temperature only, and the curve fits in [22] were used to provide a small data base for the gas mixture. Polynomial expressions for $h/e = P/(\rho e) + 1$, temperature, and internal energy were fitted to this data base. The generic polynomial was

$$Y = c_0 + c_1 X + c_2 X^2 + c_3 X^3 + c_4 X^4 + c_5 X^5 \ , \tag{12}$$

and the fitted coefficients are given in Table 5. Outside their fitted ranges, estimates of h/e were held constant while T and e were linearly extrapolated.

B Quasi-One-Dimensional Formulation

The governing equations for quasi-one-dimensional inviscid flow without heat addition are formulated with respect to the finite volume shown in Fig. 26. The geometry is specified as a set of N cells separated by interfaces located at $x_{j+\frac{1}{2}}$, $j = 0...N$ with areas $A_{j+\frac{1}{2}}$. Note that $x_{j+\frac{1}{2}} = x_{(j+1)-\frac{1}{2}}$. The volume of cell j is

$$V_j = \frac{1}{2}\left(A_{j+\frac{1}{2}} + A_{j-\frac{1}{2}}\right)\left(x_{j+\frac{1}{2}} - x_{j-\frac{1}{2}}\right) . \tag{13}$$

The flow solution is recorded as cell averages of density ρ_j, velocity u_j, and specific internal energy e_j.

The differential equations governing the conservation of mass, momentum, and total energy are approximated by

$$\frac{\partial}{\partial t}(\rho)_j = -\frac{1}{V_j}\left[\rho_{j+\frac{1}{2}} u_{j+\frac{1}{2}} A_{j+\frac{1}{2}} - \rho_{j-\frac{1}{2}} u_{j-\frac{1}{2}} A_{j-\frac{1}{2}}\right] , \tag{14}$$

$$\begin{aligned}\frac{\partial}{\partial t}(\rho u)_j = -\frac{1}{V_j}\Big[&(P_{j+\frac{1}{2}} A_{j+\frac{1}{2}} - P_{j-\frac{1}{2}} A_{j-\frac{1}{2}}) \\ &+ P_j(A_{j+\frac{1}{2}} - A_{j-\frac{1}{2}}) \\ &- (\rho_{j+\frac{1}{2}} u^2_{j+\frac{1}{2}} - \rho_{j-\frac{1}{2}} u^2_{j-\frac{1}{2}})\Big] ,\end{aligned} \tag{15}$$

$$\begin{aligned}\frac{\partial}{\partial t}(\rho E)_j = -\frac{1}{V_j}\Big[&(P_{j+\frac{1}{2}} + \rho_{j+\frac{1}{2}} E_{j+\frac{1}{2}}) u_{j+\frac{1}{2}} A_{j+\frac{1}{2}} \\ &- (P_{j-\frac{1}{2}} + \rho_{j-\frac{1}{2}} E_{j-\frac{1}{2}}) u_{j-\frac{1}{2}} A_{j-\frac{1}{2}}\Big] ,\end{aligned} \tag{16}$$

where the total energy $E = e + \frac{1}{2}u^2$, and $P = P(\rho, e)$ is the equation of state described in Appendix A. These conservation equations are integrated forward in time with a predictor-corrector technique, while interface values (with subscripts $\pm\frac{1}{2}$) are evaluated in a stable manner with an Osher-type Riemann solver [25].

At the start of each time step, the state of the flow (consisting of a set of values for ρ, u, e, P, a) either side of each interface is interpolated from the set of cell averaged states by assuming piecewise linear variation of the variables within cells. The slopes of these linear segments are limited by the nonlinear SUPERBEE limiter [26]. The Riemann solver then assumes that a spatially constant left state (subscript L) and right state (subscript R) interact through a pair of finite-amplitude compression or rarefaction waves. Perfect gas

relations [34] are used to obtain the states (L^*, R^*) in the gas after the passage of left-moving and right-moving waves, respectively. The expressions implemented in the code are

$$P_L^* = P_R^* = P_L \left[\frac{(\gamma - 1)(\overline{U}_L - \overline{U}_R)}{2a_L(1 + Z)} \right]^{2\gamma/(\gamma-1)} , \tag{17}$$

and

$$u_L^* = u_R^* = \frac{\overline{U}_L Z + \overline{U}_R}{1 + Z} , \tag{18}$$

where the Riemann invariants are

$$\begin{aligned} \overline{U}_L &= u_L + \frac{2a_L}{\gamma - 1} , \text{ and} \\ \overline{U}_R &= u_R - \frac{2a_R}{\gamma - 1} , \end{aligned} \tag{19}$$

and the intermediate variable Z is given by

$$Z = \frac{a_R}{a_L} \left(\frac{P_L}{P_R} \right)^{(\gamma-1)/(2\gamma)} . \tag{20}$$

Given the pressure and velocity in the regions behind the waves, the other flow properties may be evaluated. Sound speeds are evaluated from the invariants (19) as

$$\begin{aligned} a_L^* &= (\overline{U}_L - u_L^*)\,(\gamma - 1)/2 , \text{ and} \\ a_R^* &= (u_R^* - \overline{U}_R)\,(\gamma - 1)/2 . \end{aligned} \tag{21}$$

The specific internal energy is obtained from

$$\begin{aligned} e_L^* &= \frac{(a_L^*)^2}{\gamma(\gamma - 1)} , \text{ and} \\ e_R^* &= \frac{(a_R^*)^2}{\gamma(\gamma - 1)} , \end{aligned} \tag{22}$$

and the density is obtained from the equation of state as

$$\begin{aligned} \rho_L^* &= \frac{P_L}{(\gamma - 1)e_L^*} , \text{ and} \\ \rho_R^* &= \frac{P_R}{(\gamma - 1)e_R^*} . \end{aligned} \tag{23}$$

If the pressure rises across the left-moving wave, it is assumed to be a shock and its velocity relative to the initial left state is given by

$$u_L - w_L = \left[\frac{\gamma + 1}{2} \frac{P_L}{\rho_L} \left(\frac{P_L^*}{P_L} + \frac{\gamma - 1}{\gamma + 1} \right) \right]^{1/2} , \tag{24}$$

else, it is assumed to be a rarefaction with relative velocity

$$u_L - w_L = a_L \,. \tag{25}$$

Here w_L is the velocity of the wave relative to the cell boundaries. A similar procedure is used to obtain the velocity of the right-moving wave.

In the preceding perfect gas equations (17) - (24), an effective γ was used to include real gas effects in an approximate manner and was evaluated as a density weighted function [35]

$$\gamma = f\gamma_L + (1-f)\gamma_R \,, \tag{26}$$

where

$$f = \frac{\sqrt{\rho_L}}{\sqrt{\rho_L} + \sqrt{\rho_R}} \,, \tag{27}$$

and

$$\begin{aligned} \gamma_L &= \frac{P_L}{\rho_L e_L} + 1 \,, \\ \gamma_R &= \frac{P_R}{\rho_R e_R} + 1 \,. \end{aligned} \tag{28}$$

Given the signs and relative magnitudes of the wave speeds, the interface conditions used in the conservation equations (14) - (16) may be selected or interpolated from the 4 flow states using the following logic.

if ($u^* > 0$) then

  The contact-discontinuity has moved to the right
  and the interface state is determined from the
  L and L^* states.

  if ($P^* > P_L$) then
    The left-moving wave is a shock.
    if ($w_L \geq 0$) then
      All waves have moved to the right.
      Interface state is equal to L.
    else
      Interface state is equal to L^*.
    endif
  else
    The left-moving wave is a rarefaction.
    if ($u_L - a_L \geq 0$) then
      All waves have moved to the right.
      Interface state is equal to L.
    elseif ($u_L^* - a_L^* > 0$) then
      The rarefaction straddles the interface.
      Interpolate the interface state from
      states L and L^*.
    else
      The entire rarefaction moved to the
      left of the interface.
      Interface state is equal to L^*.
    endif
  endif

else

  The contact discontinuity has moved to the left
  and the interface state is determined from the
  R and R^* states in a similar manner...

endif

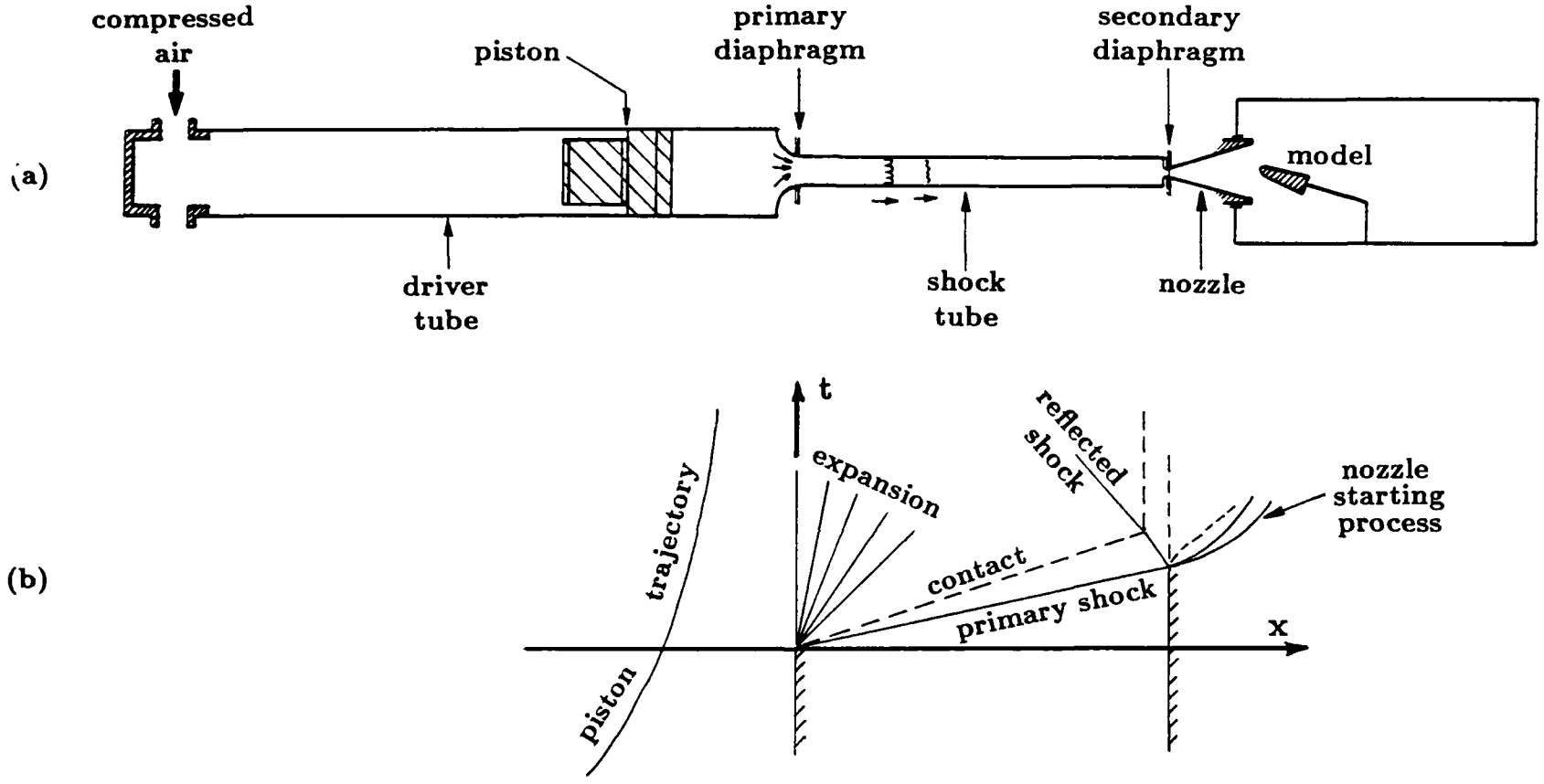

Figure 1: Reflected-shock tunnel operation. (a) Tunnel schematic, (b) $x - t$ wave diagram.

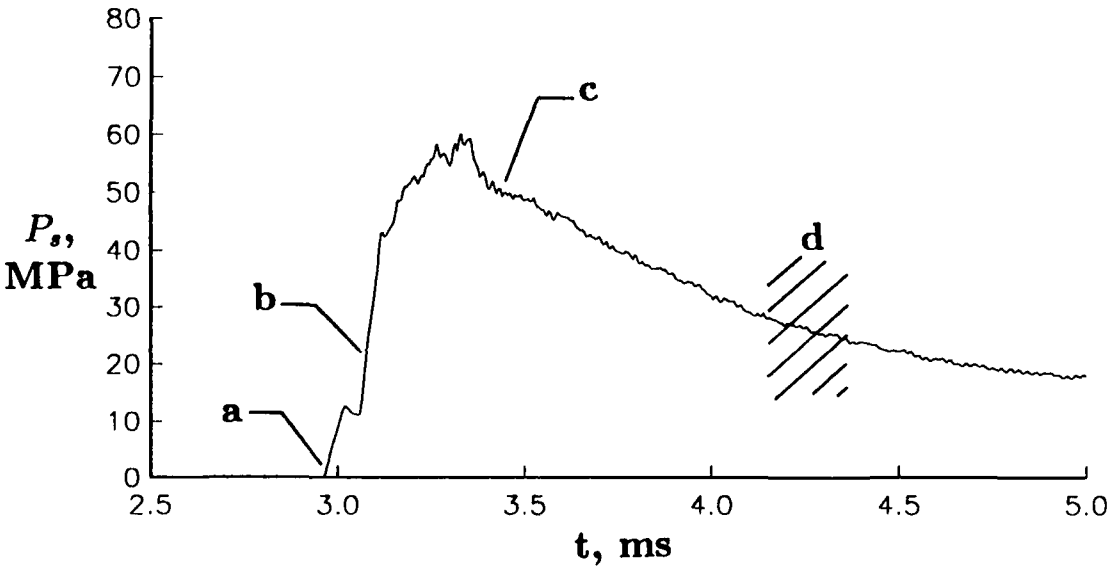

Figure 2: Typical history of the (unfiltered) nozzle supply pressure showing the principal events: (a) arrival of the incident shock; (b) reflected shock; (c) establishment of equilibrium pressure; (d) driver gas contamination.

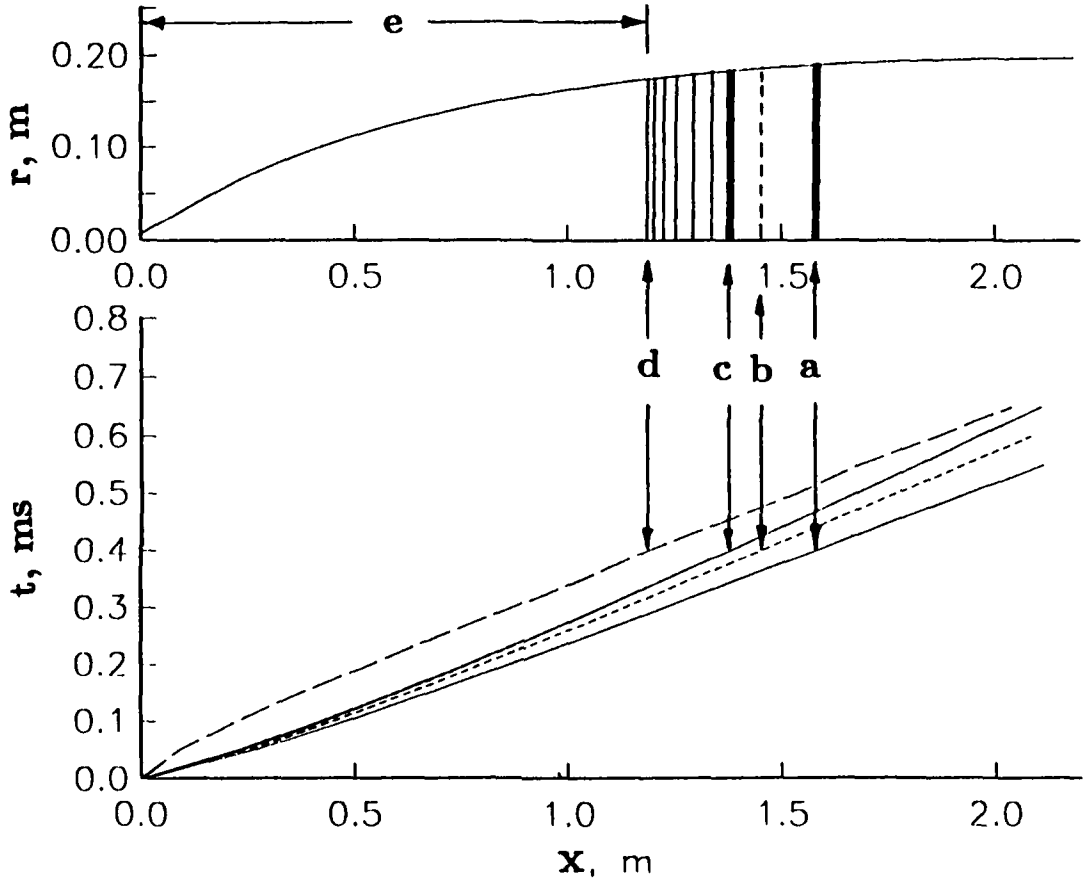

Figure 3: Quasi-one-dimensional model of the nozzle starting process in both the physical plane and the $x - t$ plane. Labelled features are: (a) primary shock; (b) contact surface; (c) upstream-facing shock; (d) upstream head of the unsteady expansion; (e) steady expansion.

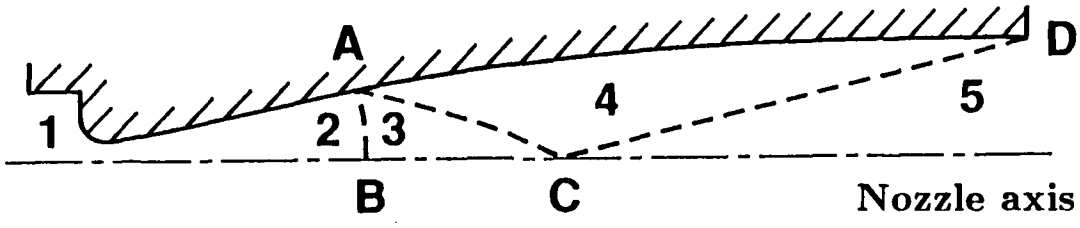

Figure 4: Schematic view of a contoured nozzle showing regions of: (1) stagnant nozzle supply gas; (2) transition to source flow; (3) source flow; (4) transition to parallel flow; (5) parallel flow.

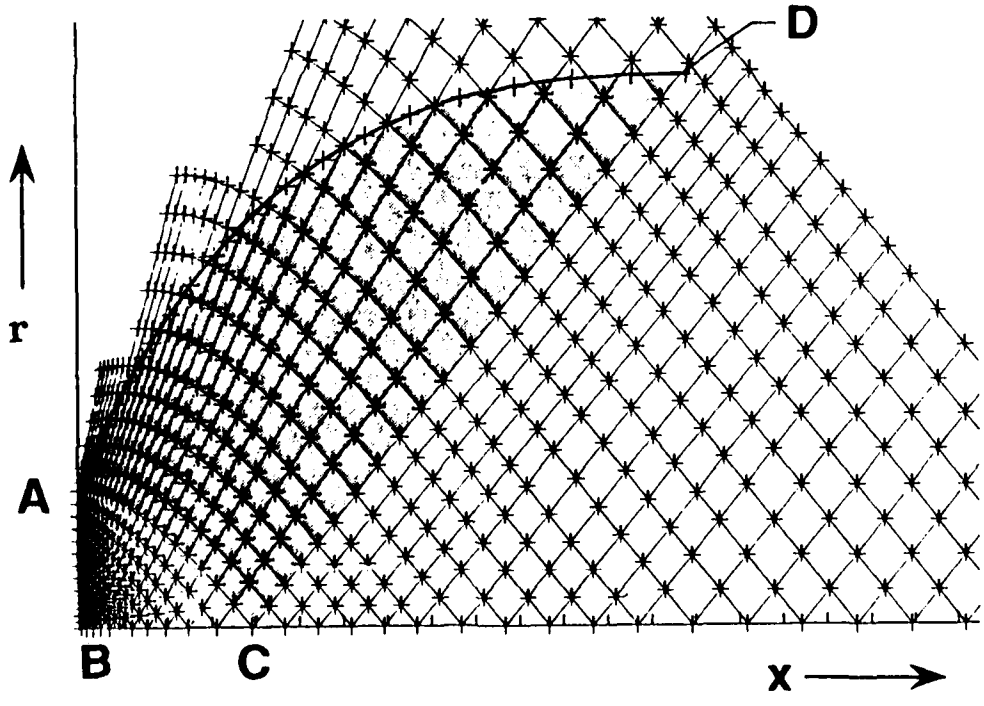

Figure 5: Characteristic mesh for regions 3, 4 and 5. The interpolated streamline extends from A to D. Note that the axial coordinate has been compressed.

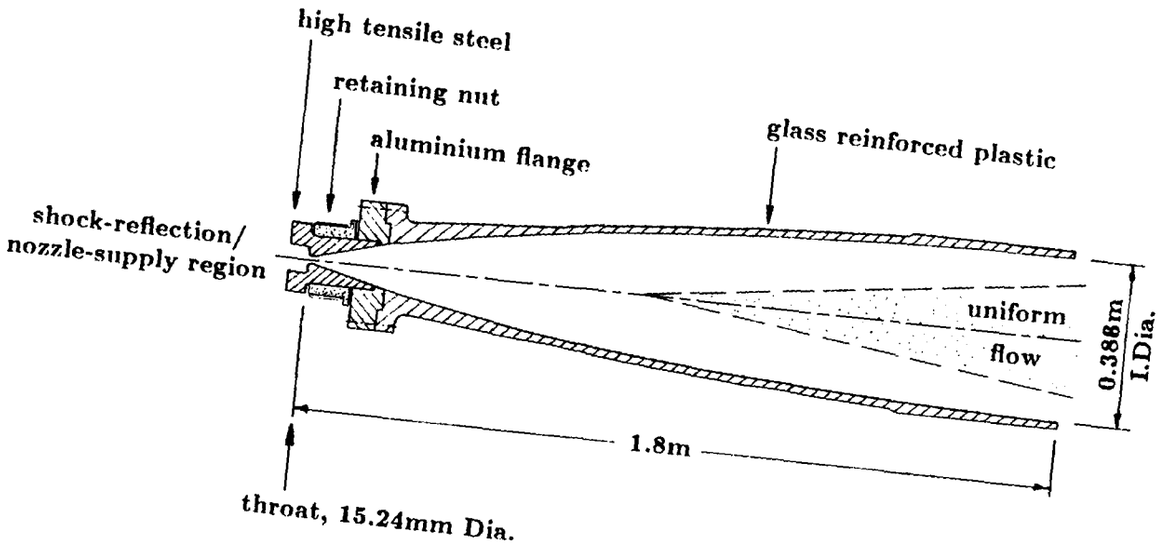

Figure 6: Sectional view of the Mach 8 nozzle.

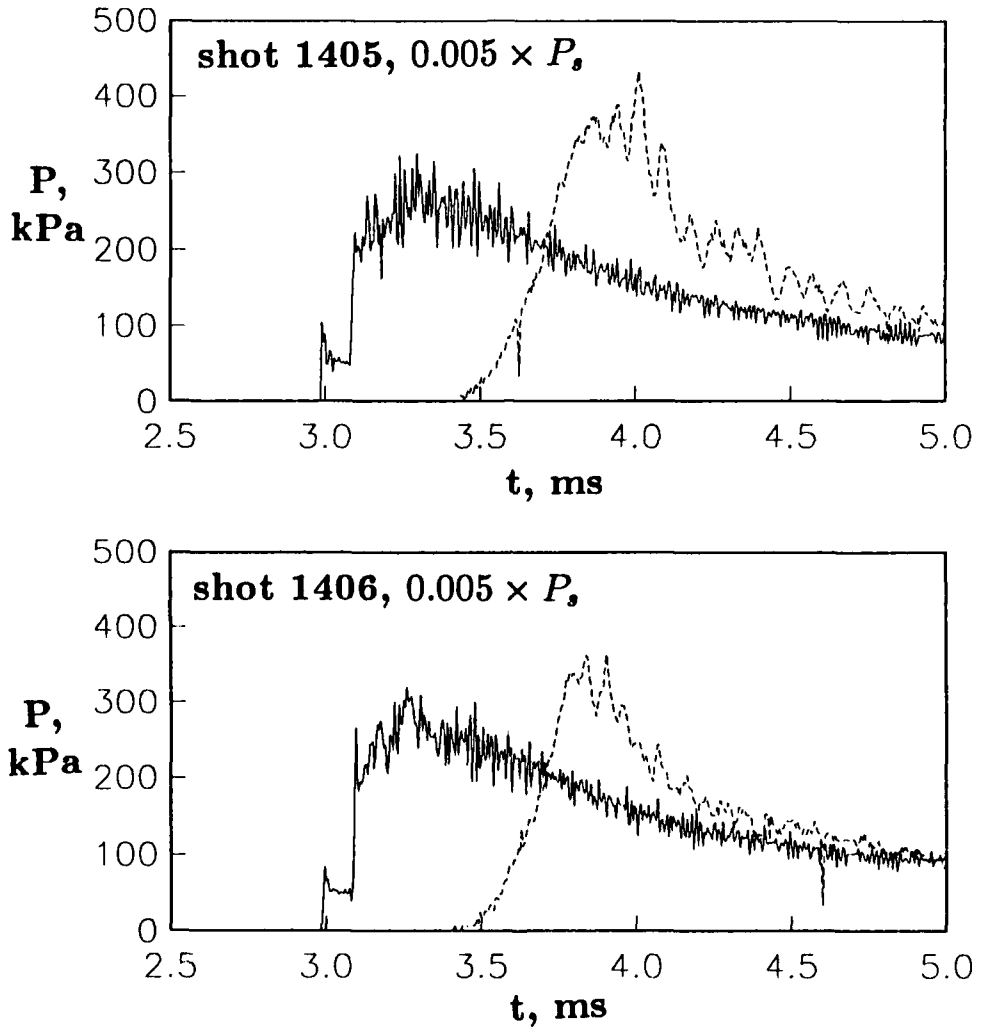

Figure 7: Typical histories for the nozzle supply pressure (solid line) and the Pitot pressure at $x \simeq 1.8m$, $r \simeq 0$ (dashed line). These traces are unfiltered.

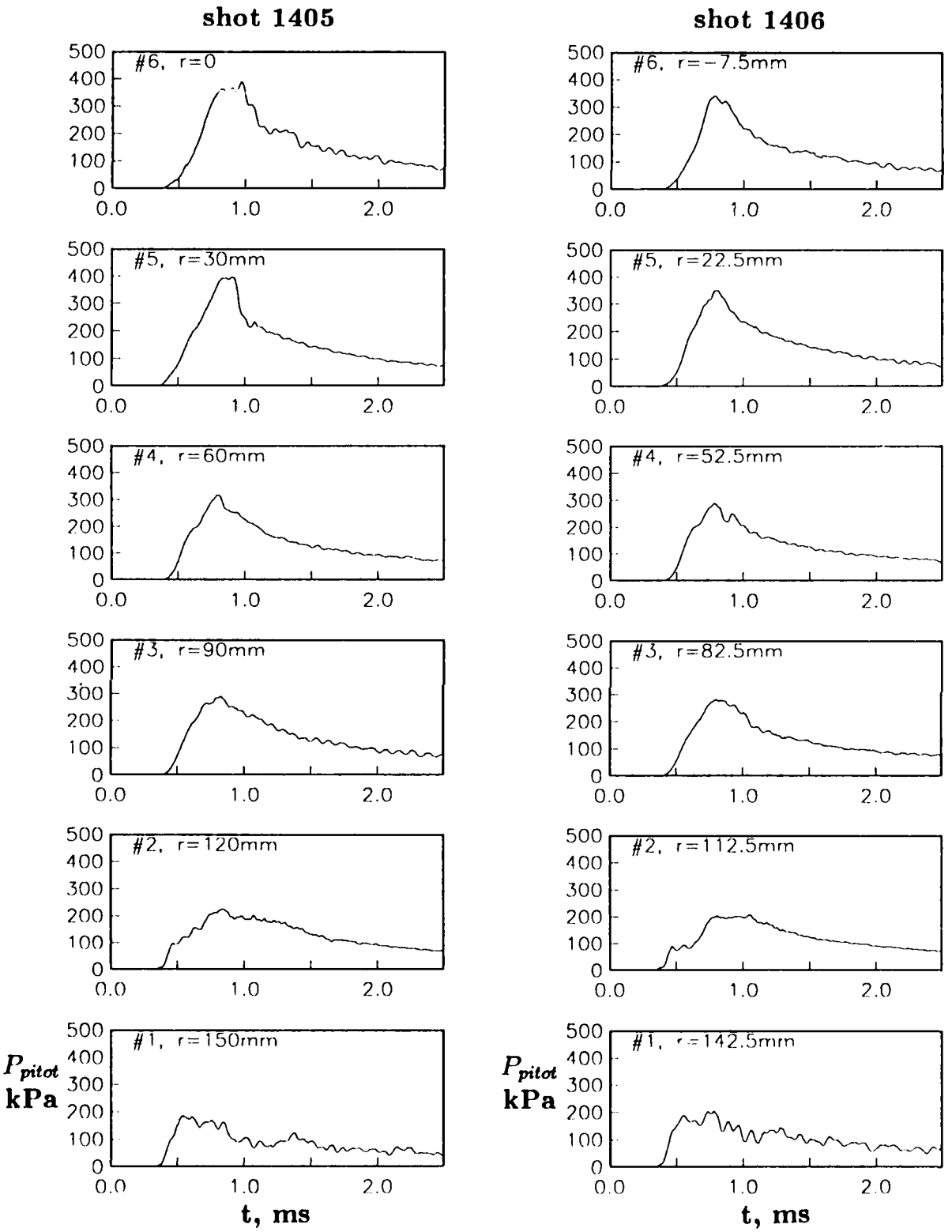

Figure 8: Filtered Pitot pressure histories at $x \simeq 1.8m$ for shots 1405 and 1406. Note that the time base has been shifted such that shock reflection occurs at $t = 0$.

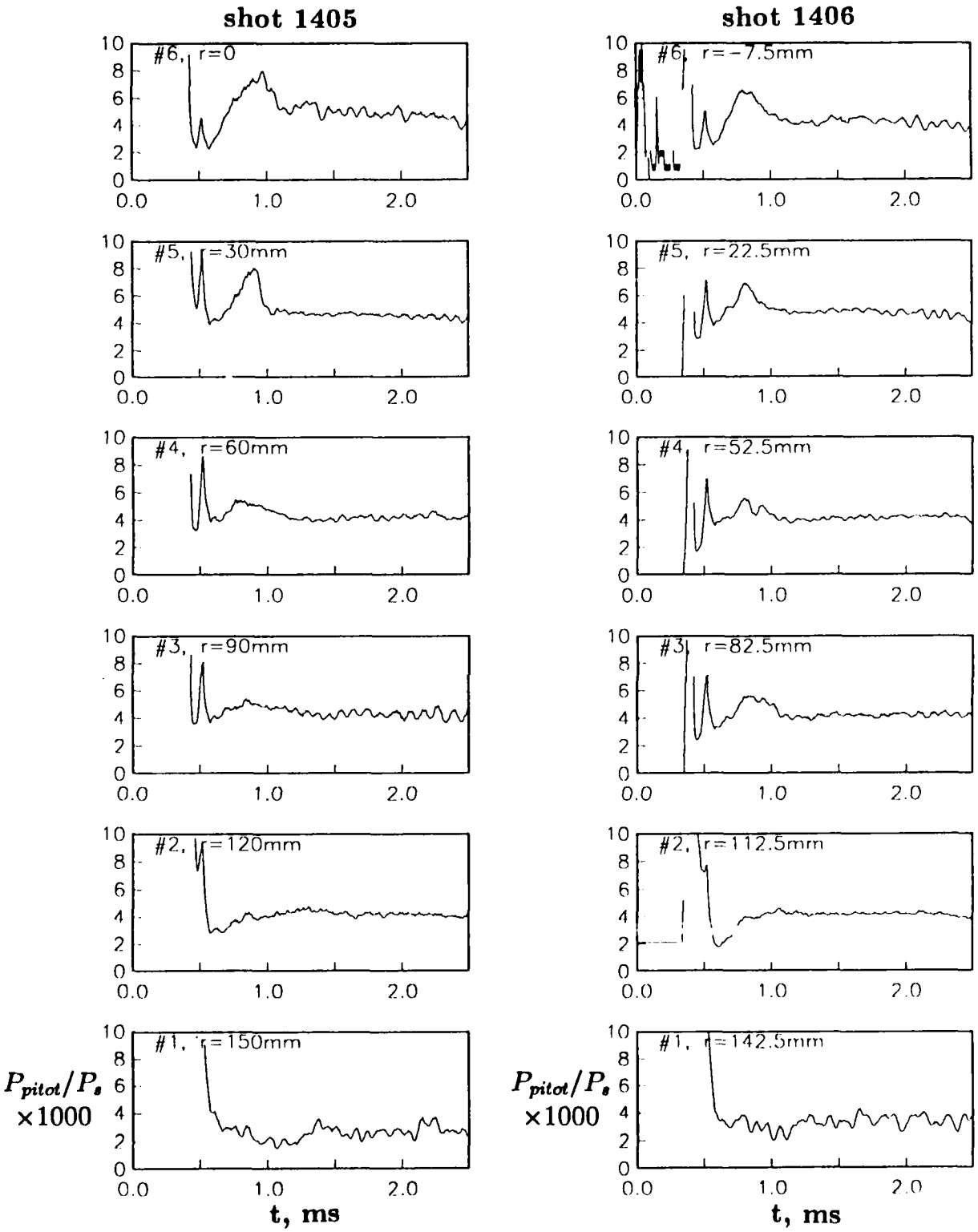

Figure 9: Normalized Pitot pressure histories at $x \simeq 1.8m$ for shots 1405 and 1406.

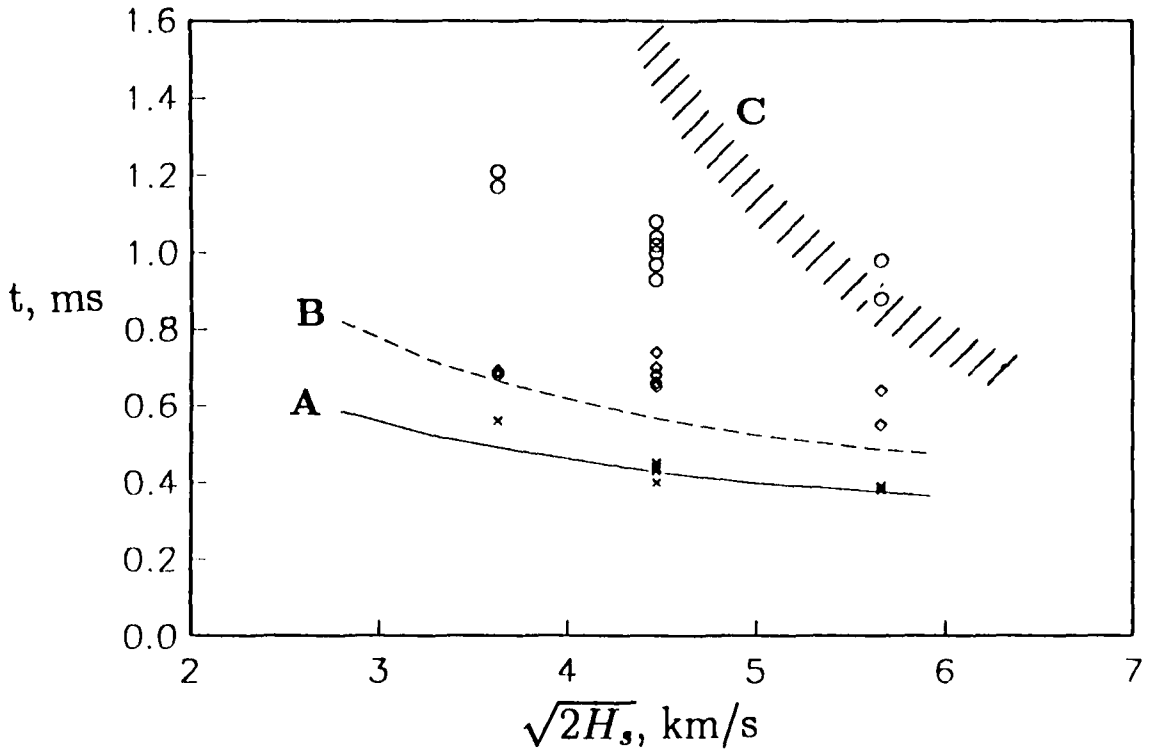

Figure 10: Times at which events occur at the nozzle exit plane for a $4mm$ primary diaphragm and $\lambda = 60$. A. primary shock arrival (Q1D model); B. settling time (10%, Q1D model); C. contamination by driver gas; $\times$ primary shock arrival (experimental); $\bigcirc$ settling time (experimental); $\diamond$ passage of the expansion fan (experimental).

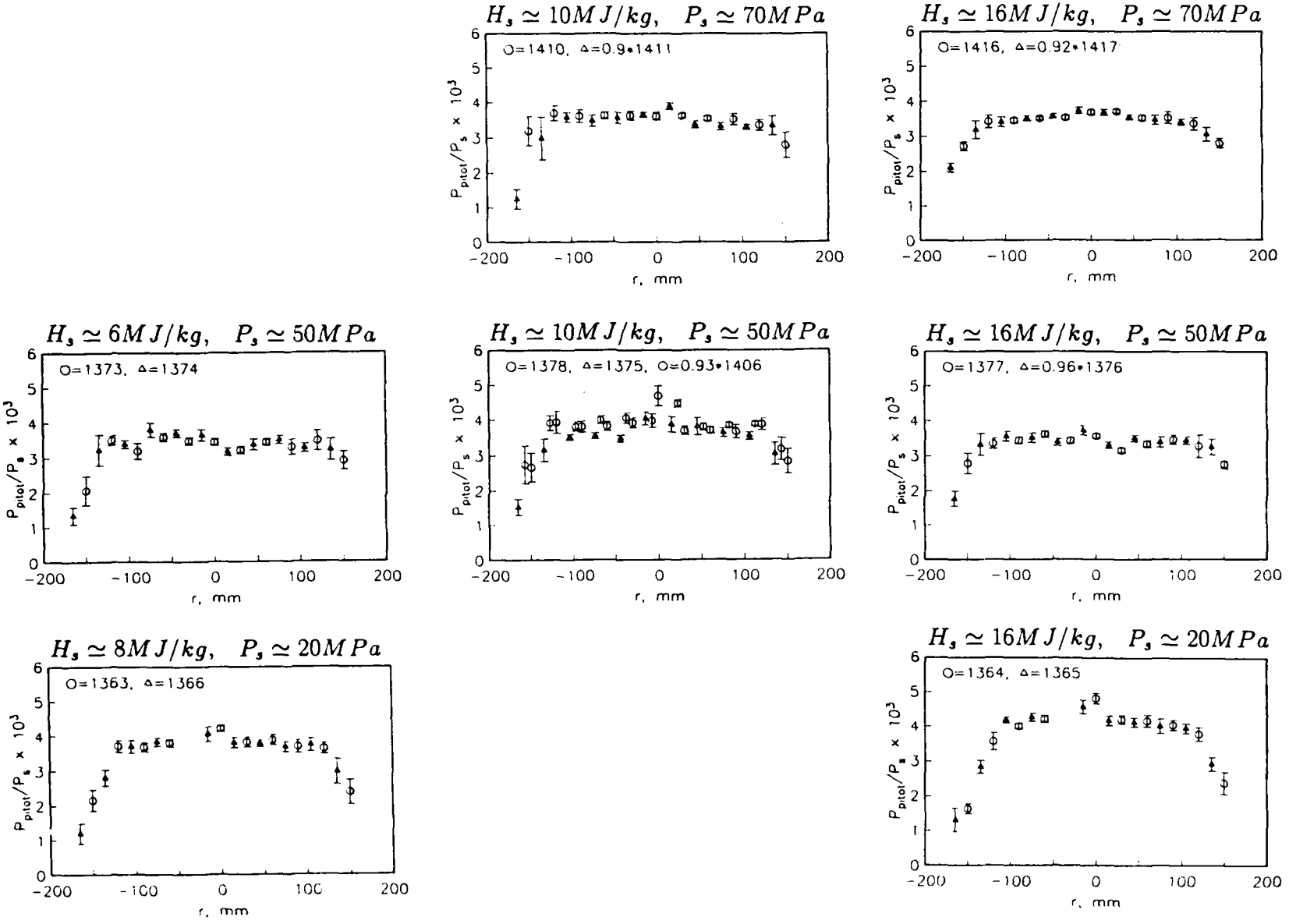

Figure 11: Quasi-steady Pitot pressure profiles at $x \simeq 1.8m$.

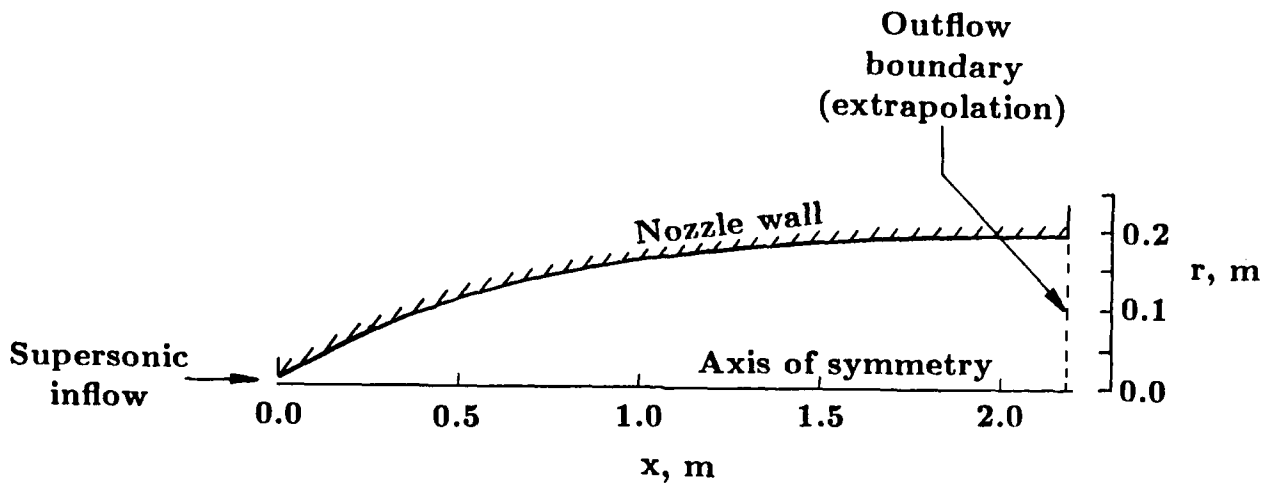

Figure 12: Flow geometry for the numerical simulations.

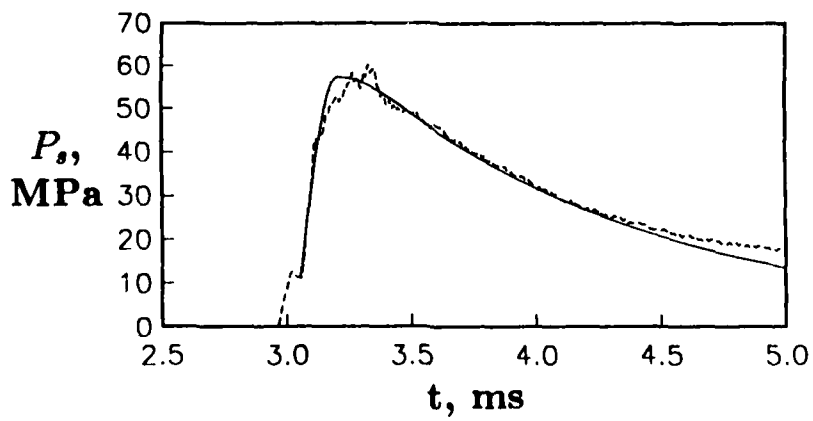

Figure 13: Transient supply pressure. Dashed line: filtered P_s for shot 1405; Solid line: transient inflow approximation.

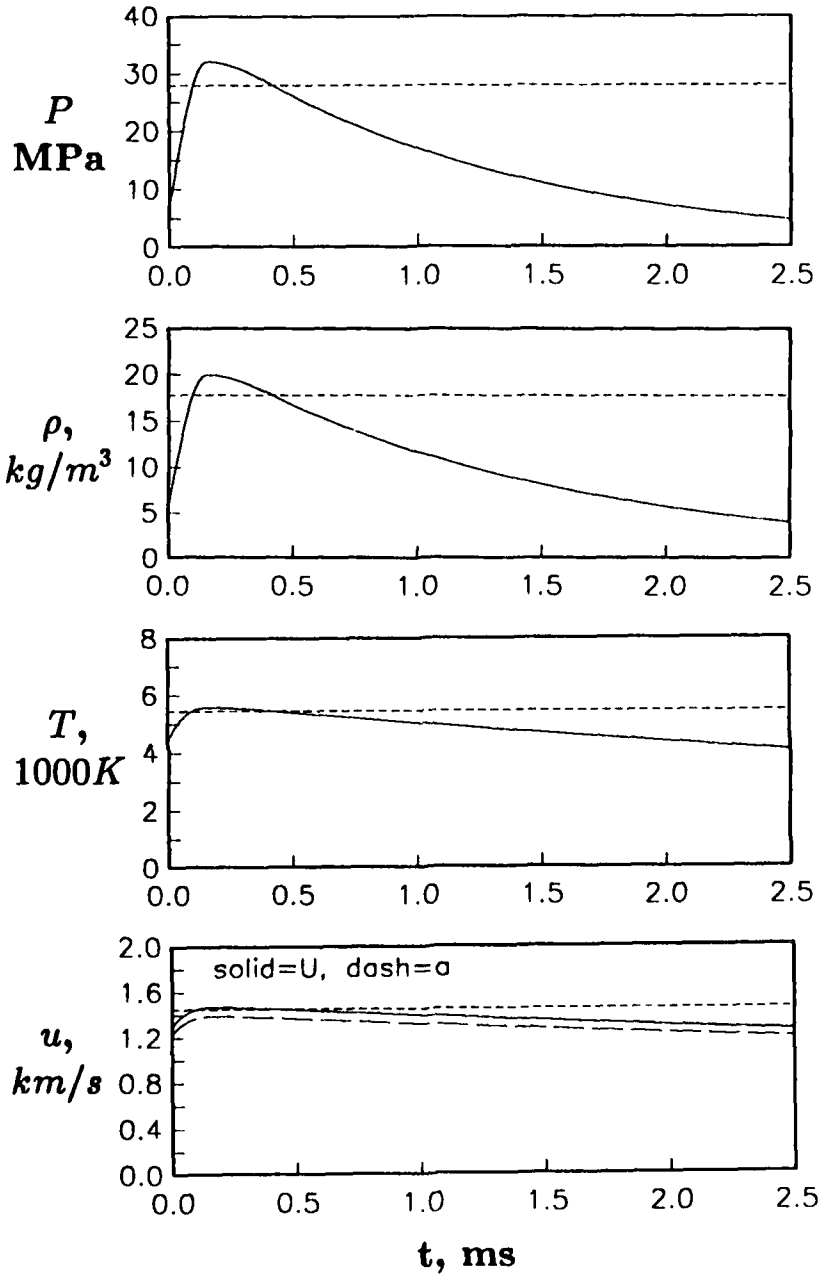

Figure 14: Transient throat conditions. Dashed lines show the steady inflow conditions.

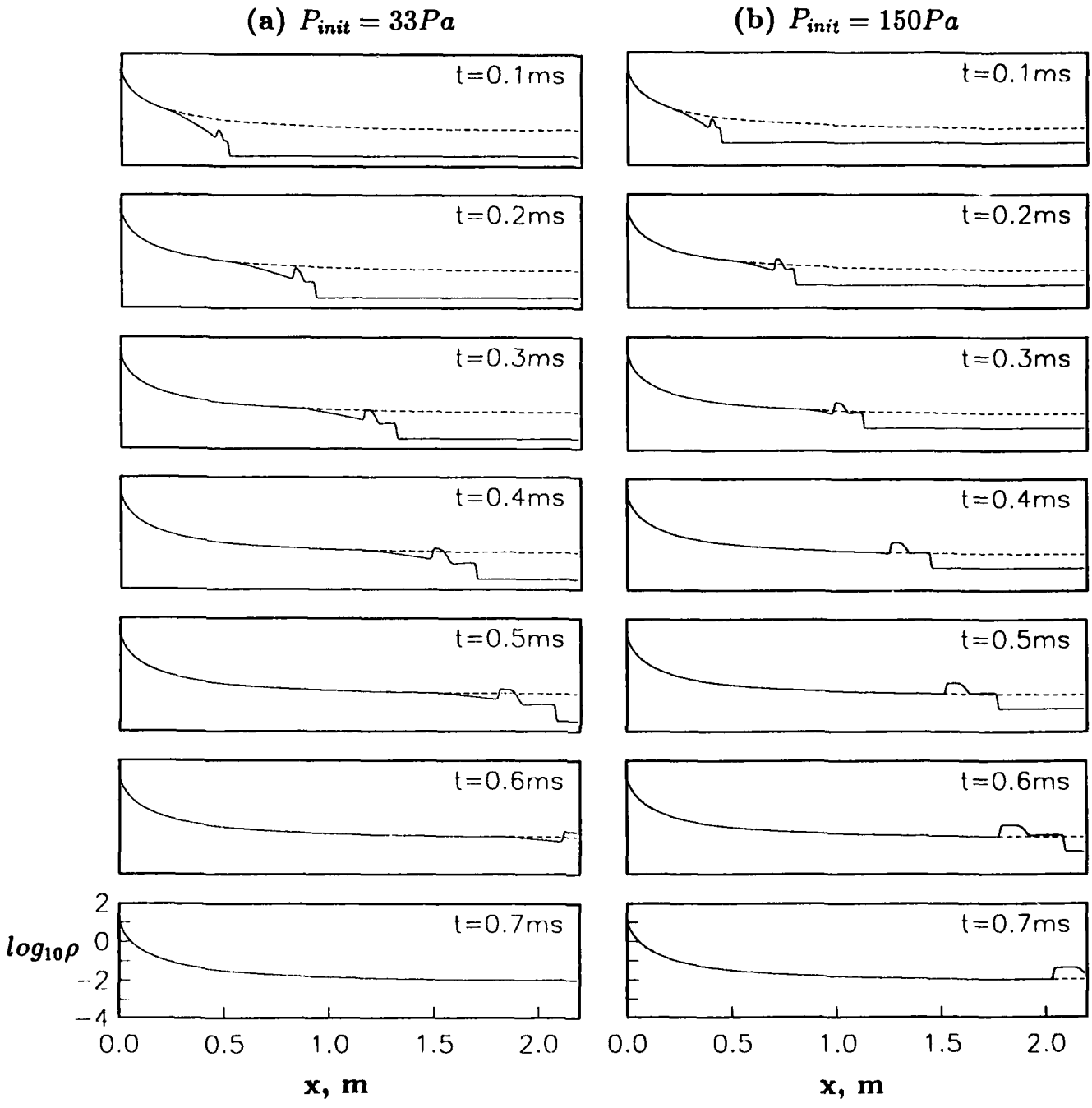

Figure 15: Evolution of the density profile for (a) $P_{init} = 33Pa$, (b) $P_{init} = 150Pa$. Solid lines are for the times as shown. Dashed lines show the solution at $t = 1.2ms$.

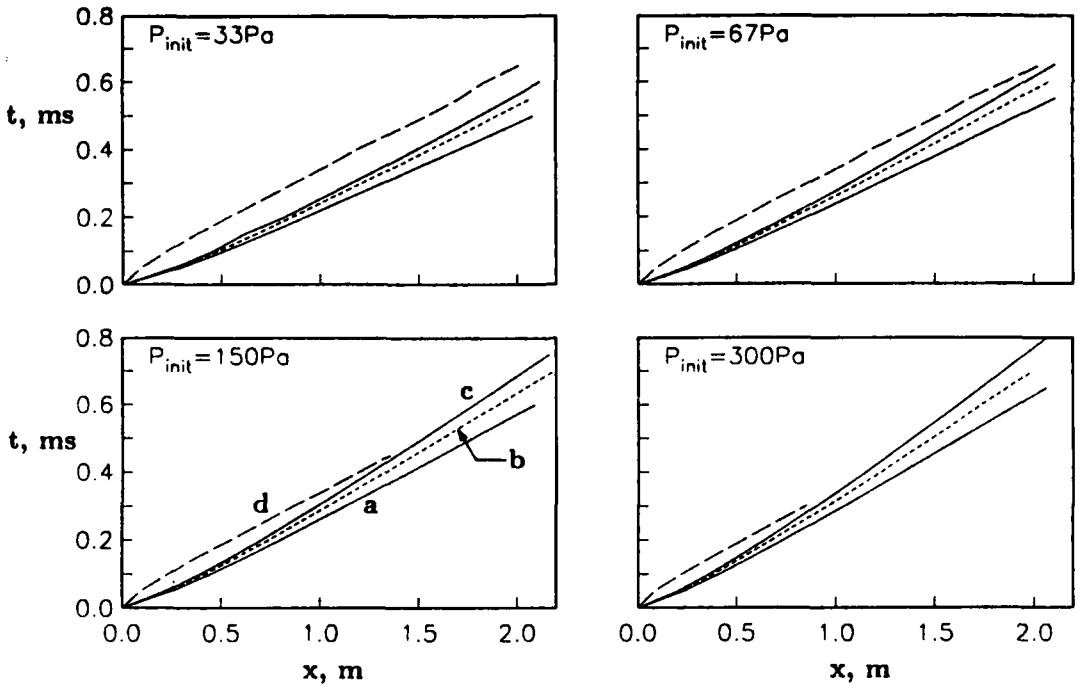

Figure 16: Wave diagrams for various initial pressures showing: (a) primary shock; (b) contact surface; (c) upstream-facing shock; (d) upstream head of the unsteady expansion.

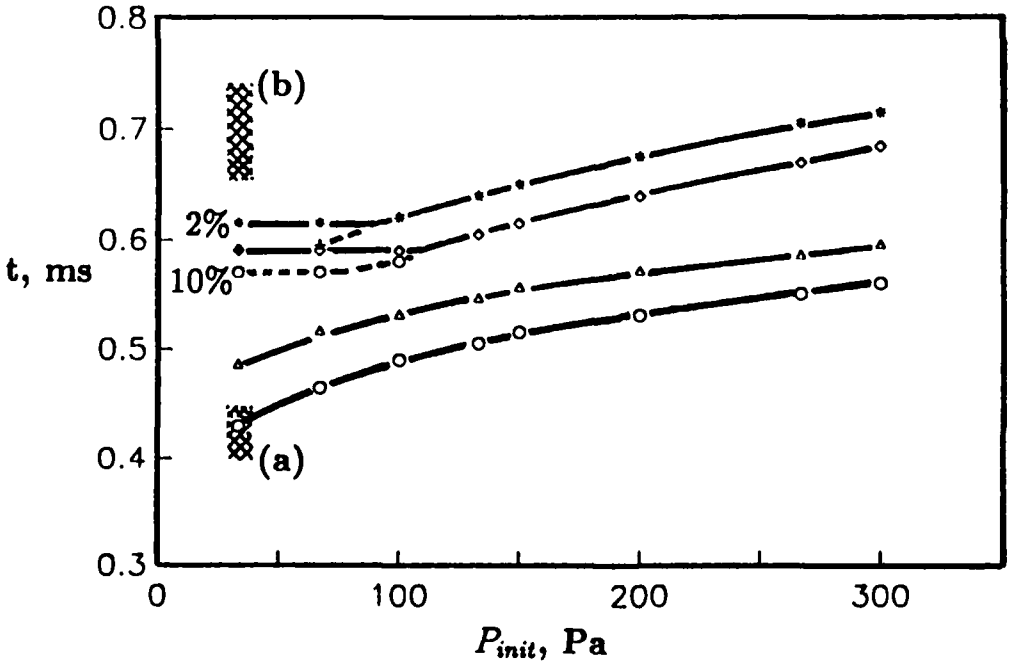

Figure 17: The variation of event times with initial pressure. ◇ settling time (10%) for steady inflow; * settling time (10%) - transient inflow; ○ primary shock passage for steady inflow; △ primary shock passage for transient inflow. Hatched areas show the estimated experimental times for (a) primary shock arrival and (b) arrival of the upstream-head of the unsteady expansion.

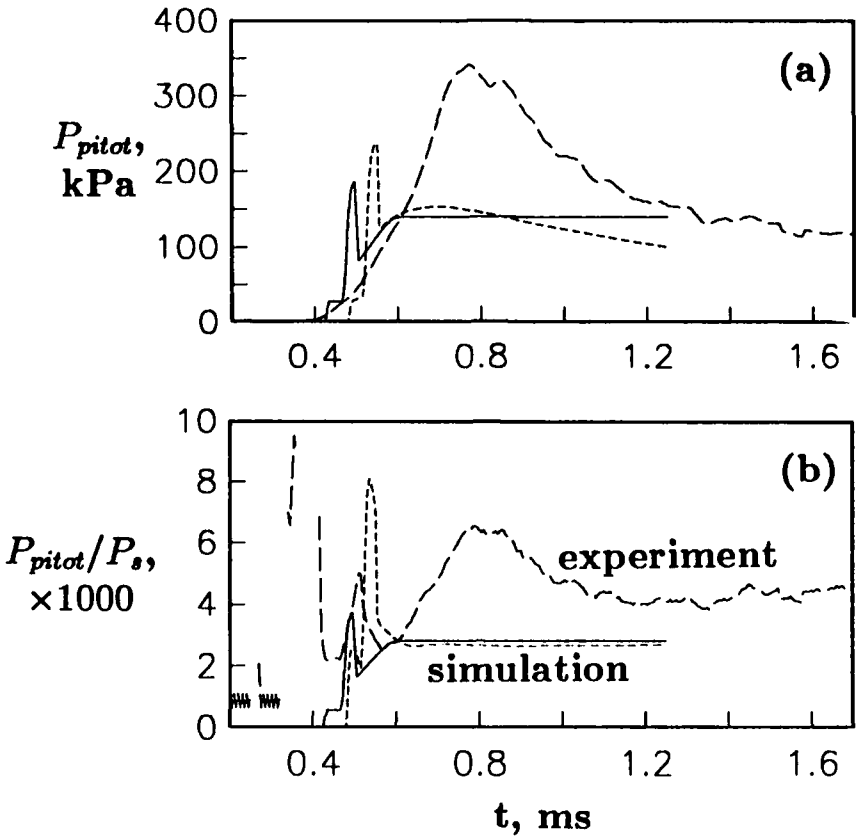

Figure 18: Comparison of (a) raw and (b) normalized Pitot pressure histories and experimental data for $r = 7.5mm$, shot 1406: solid line = steady throat conditions; short dash = transient throat conditions; long dash = experiment.

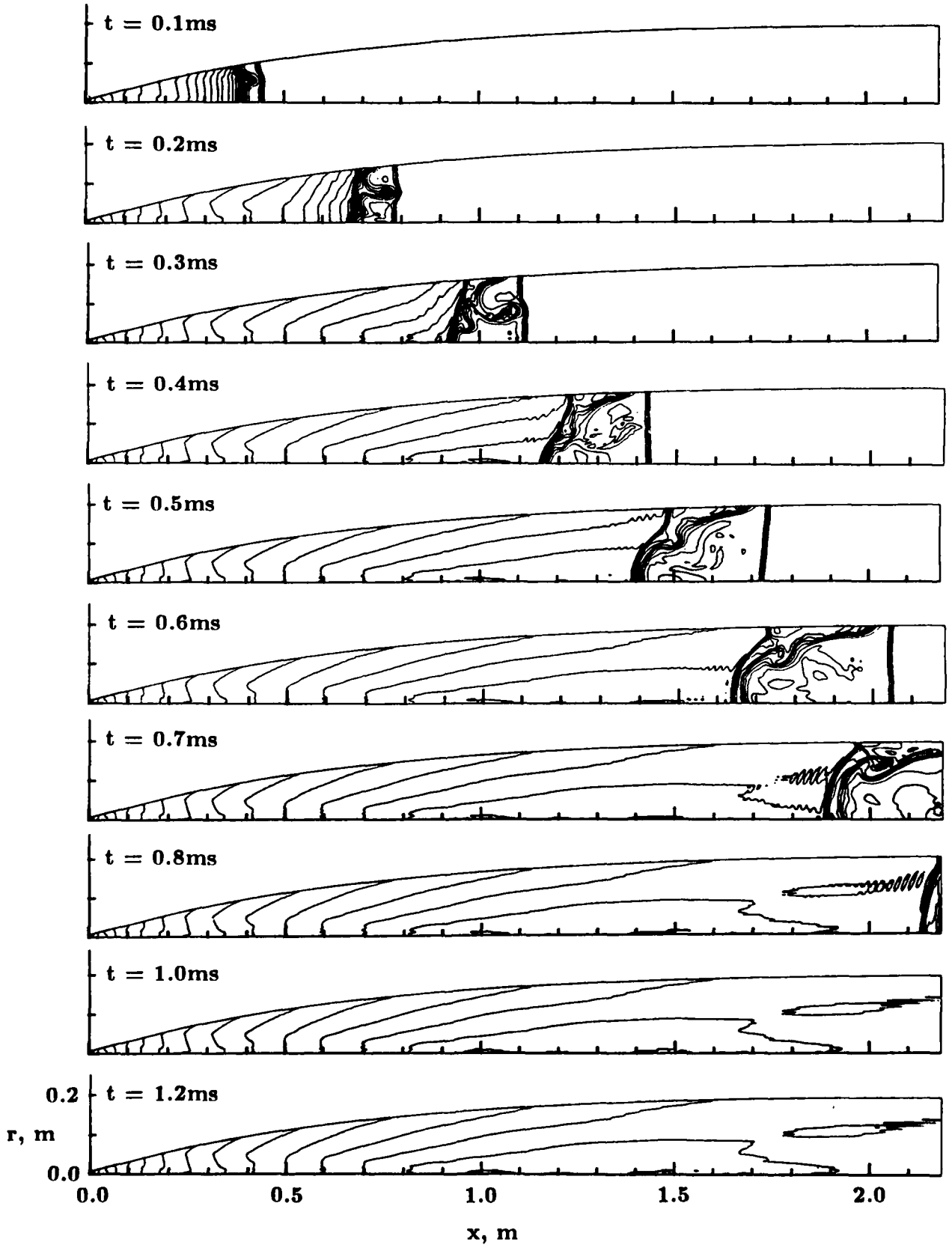

Figure 19: Mach number contours showing the axisymmetric starting process with an inviscid-wall boundary condition. (Contour levels every 0.5.)

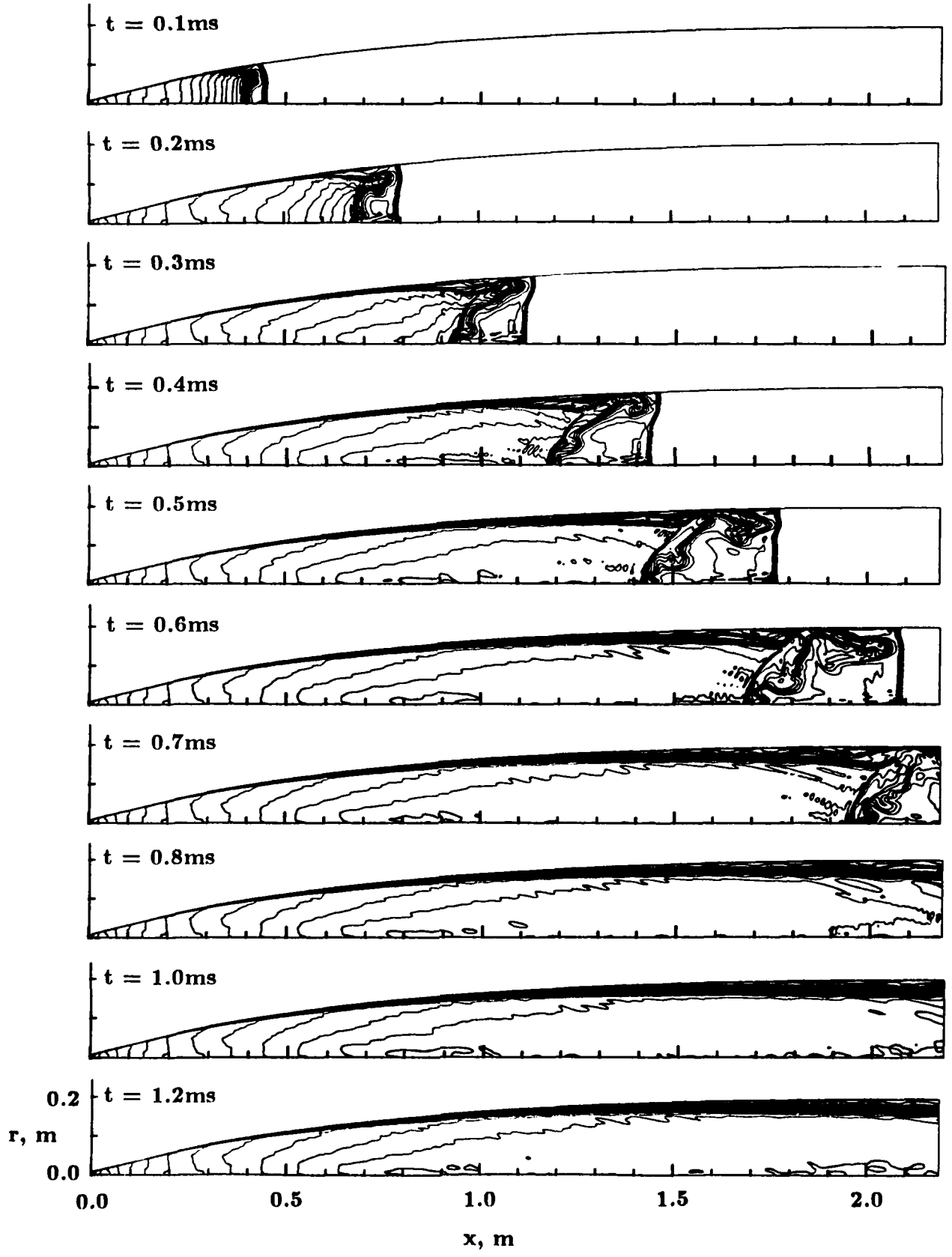

Figure 20: Mach number contours showing the axisymmetric starting process with a viscous-wall boundary condition. (Contour levels every 0.5.)

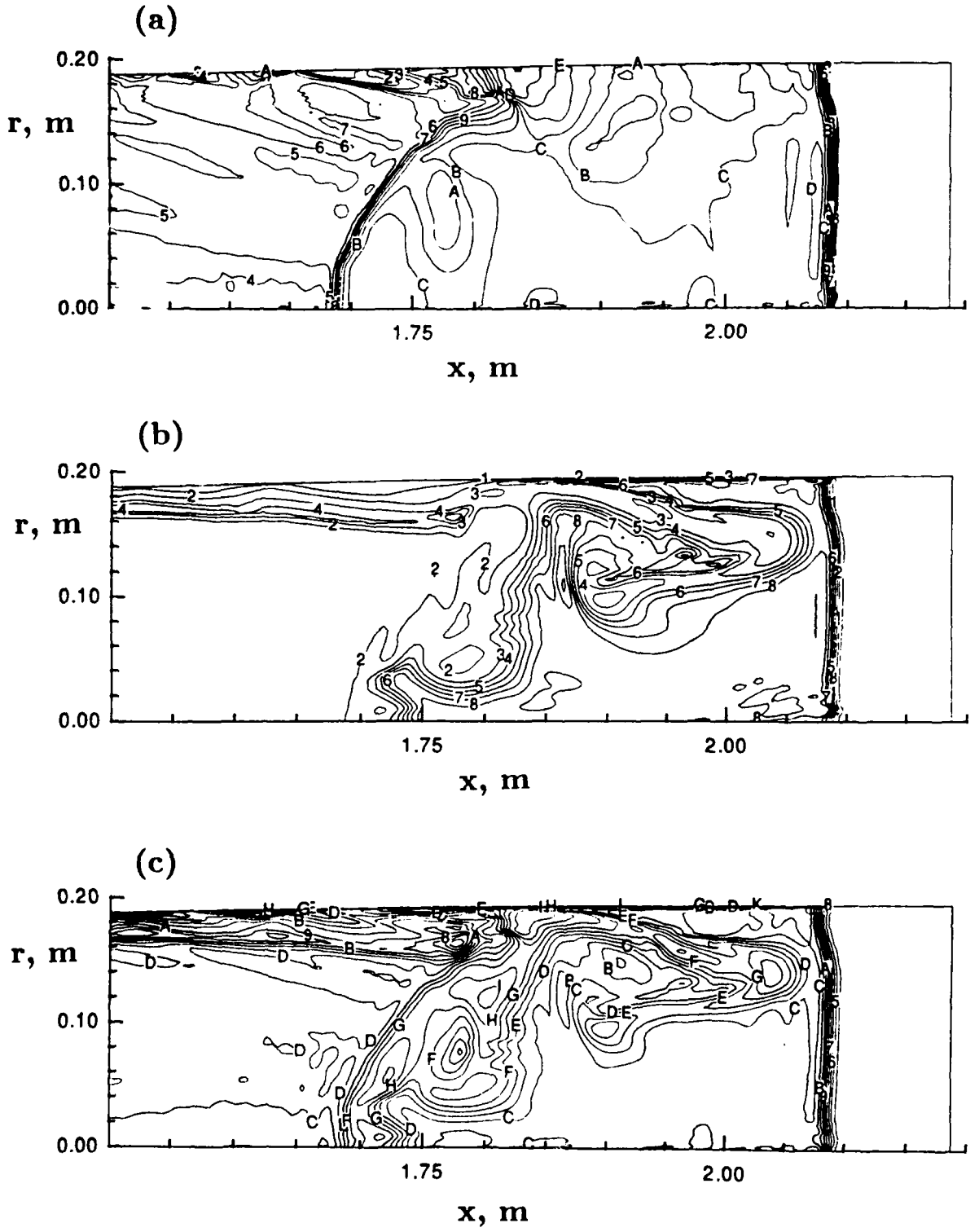

Figure 21: Details of the shock structure for the viscous-wall simulation at $t = 0.6ms$. (a) log_{10}(static pressure, Pa), contour levels every 0.1; (b) static temperature, contour levels every $500°K$; (c) log_{10}(density, kg/m^3), contour levels every 0.1.

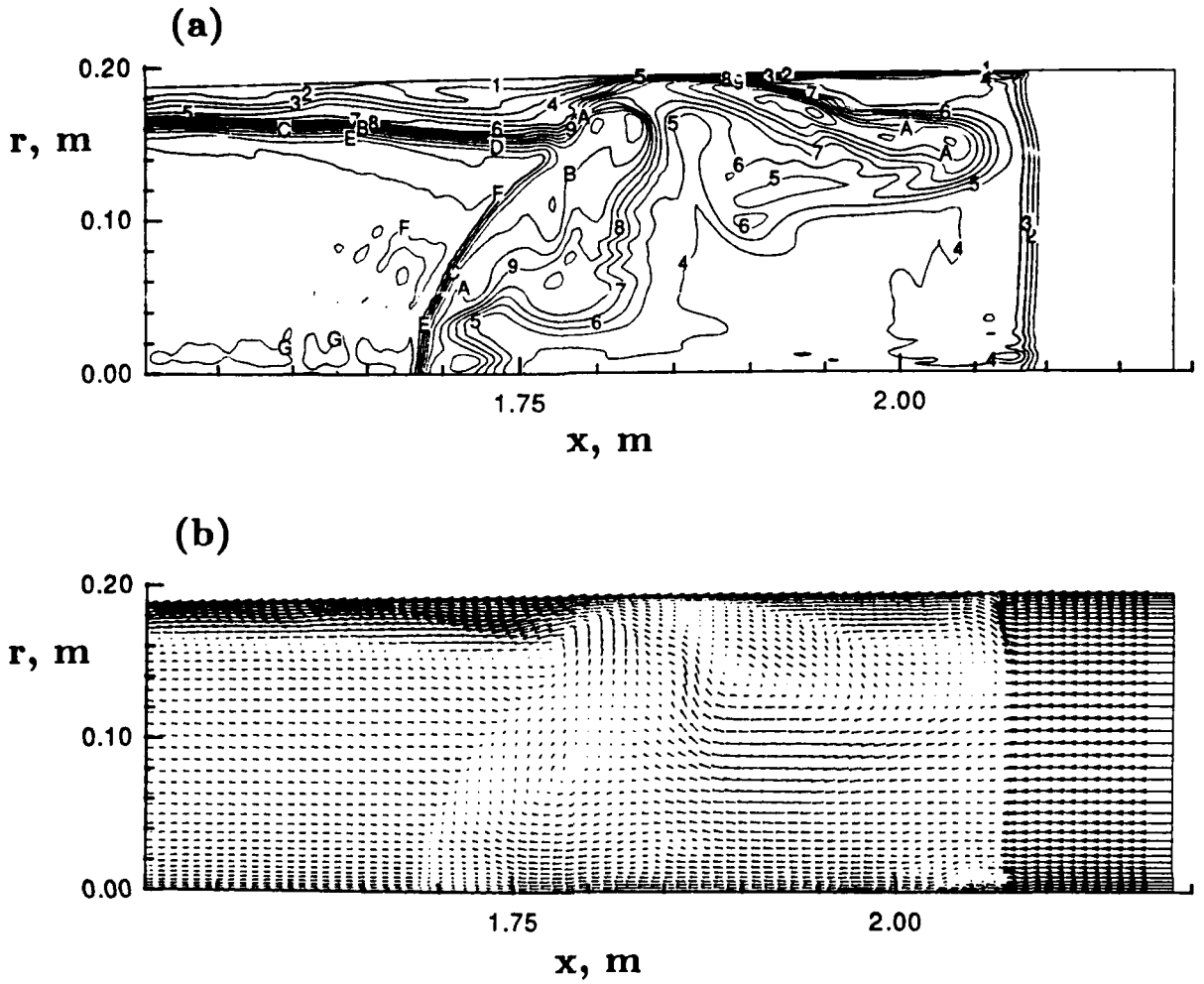

Figure 22: Details of the shock structure for the viscous-wall simulation at $t = 0.6ms$. (a) Mach number, contour levels every 0.5; (b) velocity field in the frame of reference stationary with respect to the primary shock ($u \simeq 3214m/s$).

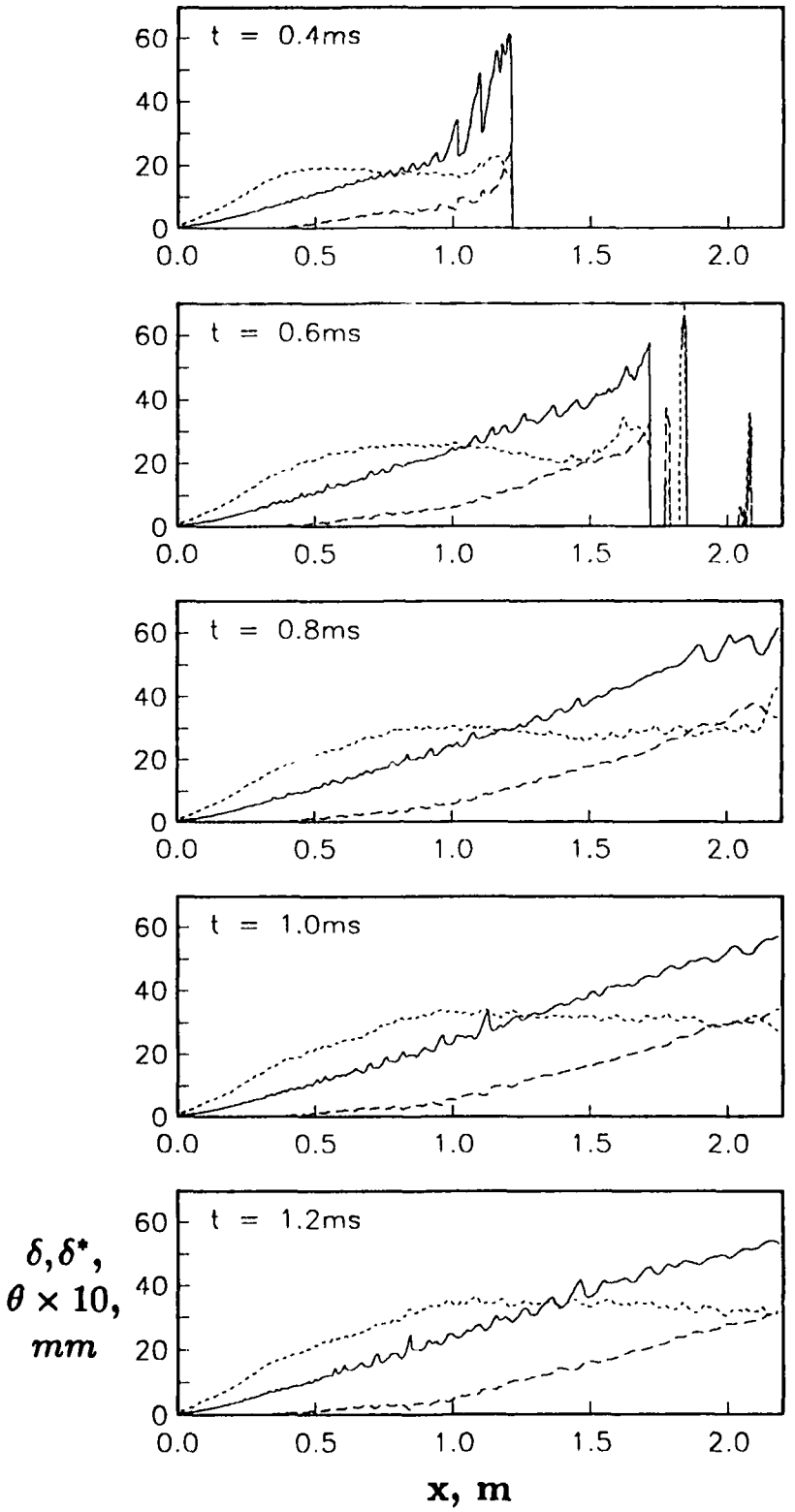

Figure 23: Boundary layer development for the viscous wall simulation: solid line = δ; long dash = δ^*; short dash = θ.

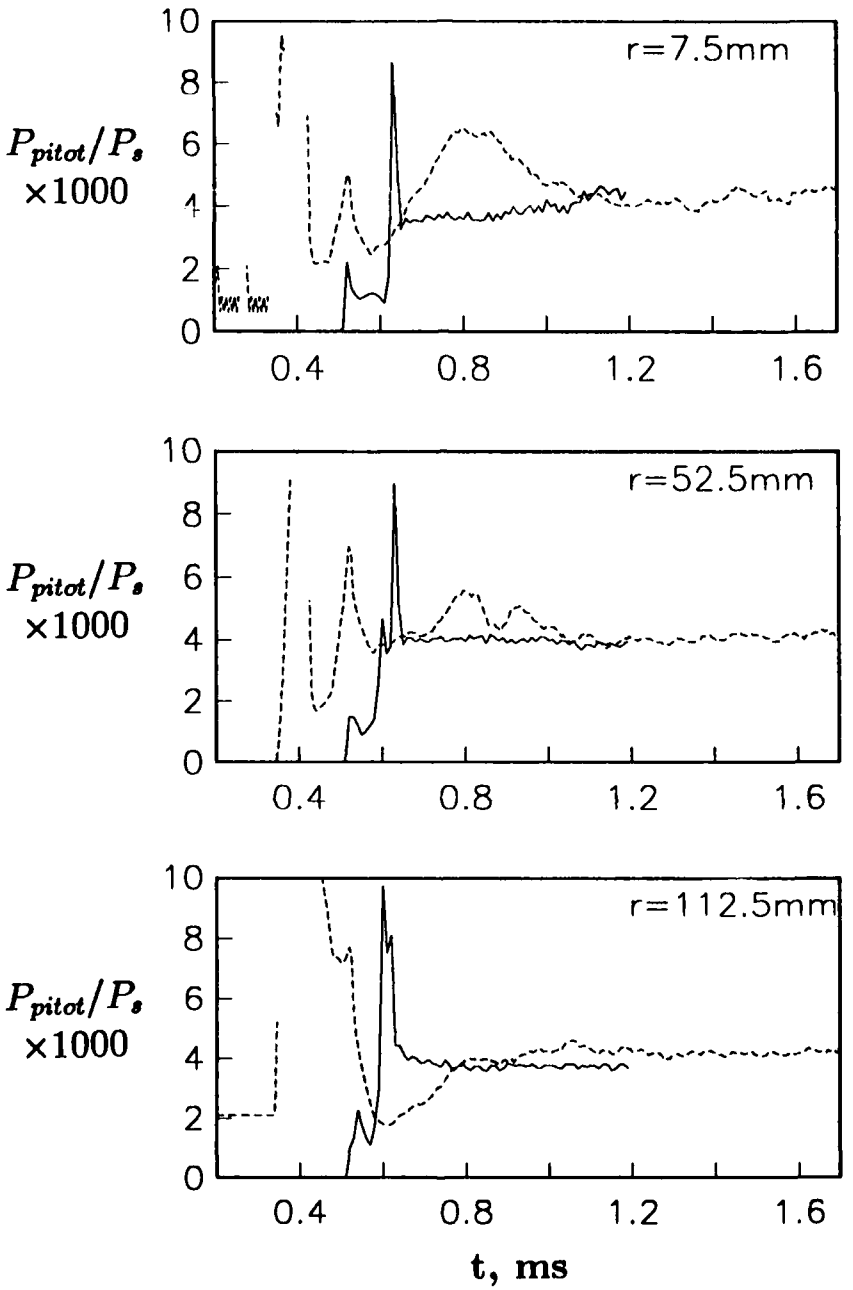

Figure 24: Comparison of normalized Pitot pressure histories for the viscous-wall simulation and shot 1406: solid line = simulation; dash = experiment.

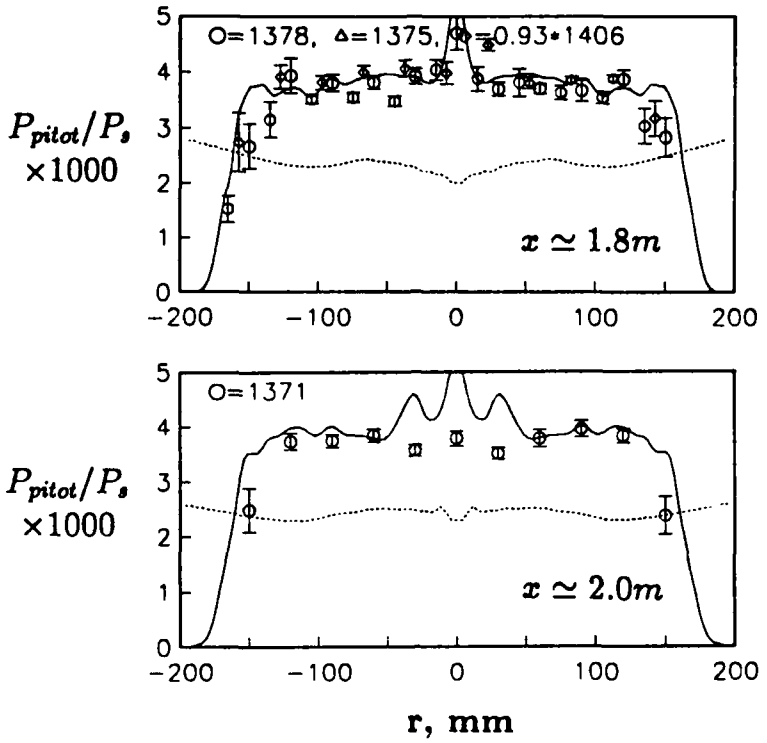

Figure 25: Quasi-steady normalized Pitot pressures across the nozzle exit plane ($x \simeq 1.8m$) and further downstream at $x \simeq 2.0m$: solid line = viscous-wall simulation; dash = inviscid-wall simulation.

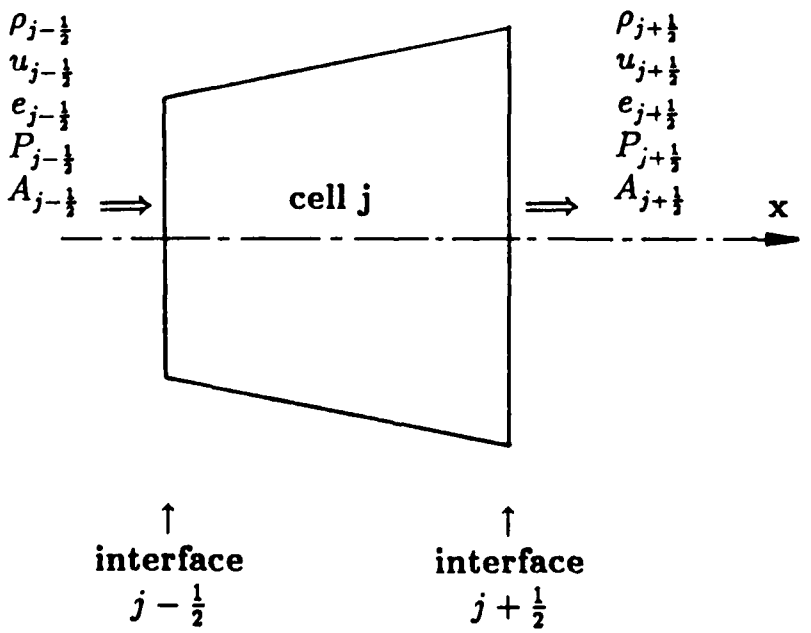

Figure 26: The generic cell used in the quasi-one-dimensional formulation.

Report Documentation Page

1. Report No.	2. Government Accession No.	3. Recipient's Catalog No.
NASA CR-187496 ICASE Report No. 91-1		

4. Title and Subtitle	5. Report Date
TRANSIENT, HYPERVELOCITY FLOW IN AN AXISYMMETRIC NOZZLE	January 1991
	6. Performing Organization Code

7. Author(s)	8. Performing Organization Report No.
P. A. Jacobs	91-1
	10. Work Unit No.
	505-90-21-01

9. Performing Organization Name and Address	11. Contract or Grant No.
Institute for Computer Applications in Science and Engineering Mail Stop 132C, NASA Langley Research Center Hampton, VA 23665-5225	NAS1-18605
	13. Type of Report and Period Covered
12. Sponsoring Agency Name and Address	Contractor Report
National Aeronautics and Space Administration Langley Research Center Hampton, VA 23665-5225	14 Sponsoring Agency Code

15. Supplementary Notes

Langley Technical Monitor:
Richard W. Barnwell

To be submitted as an AIAA paper.

Final Report

16. Abstract

This study examines the performance of an axisymmetric nozzle which was designed to produce uniform, parallel flow with a nominal Mach number of 8. A free-piston-driven shock tube was used to supply the nozzle with high-temperature, high-pressure test gas. Performance was assessed by measuring Pitot pressures across the exit plane of the nozzle and, over the range of operating conditions examined, the nozzle produced satisfactorily test flows. However, there were flow disturbances that persisted for significant times after flow initiation.

The detailed starting process of the nozzle was also investigated by performing numerical simulations at several nominal test conditions. The **classical** description of the starting process, based on a quasi-one-dimensional model, provided a reasonable approximation and was used to demonstrate that the starting process could consume a significant fraction of the otherwise usable test gas. This was especially important at high operating enthalpies where nozzle supply conditions were maintained for shorter times. Multidimensional simulations illustrated a mechanism by which the starting process in the actual nozzle could take longer than that predicted by the quasi-one-dimensional analysis. However, the cause of the persistent disturbances observed in the experimental calibration was not identified.

17. Key Words (Suggested by Author(s))	18. Distribution Statement
shock-tunnel, nozzle, transient-flow, hypervelocity-flow	09 - Research and Support Facilities (Air) 34 - Fluid Mechanics and Heat Transfer Unclassified - Unlimited

19. Security Classif. (of this report)	20. Security Classif. (of this page)	21 No. of pages	22 Price
Unclassified	Unclassified	52	A03